Scientific Reports

https://doi.org/10.1038/s41598-026-38175-6

Article in Press

Biocompatible 3D hierarchical flower-like iron-doped silver nanostructures as a platform for in vitro and in vivo drug delivery

Received: 24 September 2025

Accepted: 29 January 2026

Published online: 03 February 2026

Cite this article as: Almosawy W., Landarani-Isfahani A., Moghadam M. *et al.* Biocompatible 3D hierarchical flower-like iron-doped silver nanostructures as a platform for in vitro and in vivo drug delivery. *Sci Rep* (2026). https://doi.org/10.1038/s41598-026-38175-6

Wala Almosawy, Amir Landarani-Isfahani, Majid Moghadam, Shahram Tangestaninejad, Iraj Mohammadpoor-Baltork, Maryam Royvaran, Vahideh Asadi, Fatima Koteich & Valiollah Mirkhani

Biocompatible 3D Hierarchical Flower-like Iron-Doped Silver Nanostructures as a Platform for in vitro and in vivo Drug Delivery

Wala Almosawy,[1] Amir Landarani-Isfahani,[1] Majid Moghadam,[1,*] Shahram Tangestaninejad,[1,*] Iraj Mohammadpoor-Baltork,[1] Maryam Royvaran,[2] Vahideh Asadi,[1] Fatima Koteich,[1] Valiollah Mirkhani[1]

[1]*Department of Chemistry, University of Isfahan, Isfahan 81746-73441, Iran*

[2]*Kia Nano BioVista Laboratory, Tehran 14816-34615, Iran,*

* Corresponding authors.
Email addresses: moghadamm@sci.ui.ac.ir (M. Moghadam); stanges@sci.ui.ac.ir (S. Tangestaninejad)

Keywords: Hierarchical flower-like nanostructures, Iron-doped silver nanoparticles, Methotrexate (MTX), pH-responsive drug delivery, Biocompatibility study

Abstract: Nanostructured platforms have attracted significant attention as promising drug carriers due to their unique properties and therapeutic efficiency. This work aims to prepare three-dimensional flower-like iron-doped silver nanostructures (HFAg-Fe) and evaluate their potential as nanocarriers for Methotrexate (MTX), a first-generation anticancer and autoimmune drug. The HFAg-Fe were synthesized, modified, and characterized by FE-SEM, FT-IR, XRD, AFM, and elemental analyses. Drug loading and release were studied using UV–vis spectroscopy, showing an MTX loading capacity of 86% and pH-responsive behavior rapid release under acidic tumor conditions and slower release at physiological pH, potentially reducing side effects. Hemolysis and cytotoxicity assays indicated that HFAg-Fe/MTX possessed superior biocompatibility and anticancer efficacy compared to free MTX, while fluorescence microscopy confirmed efficient uptake by cells. Cell cycle analysis

showed treatment-induced arrest, mainly at the S phase. X-ray Micro-Computed Tomography revealed significant tumor volume reduction and preferential accumulation of the nanocarrier at the tumor site. These findings highlight the potential of HFAg-Fe nanostructures as safe drug delivery systems, where 4-aminothiophenol serves as a linker to facilitate drug loading and release, potentially enhancing outcomes in cancer therapy.

1. Introduction

The challenge of delivering drug molecules to target cells remains a significant issue in modern medicine. Effectively directing therapeutic drugs to specific tissues or cells through the bloodstream is difficult, which complicates the treatment of many diseases. Despite advances in drug formulation, most systemic deliveries result in non-selective distribution, reducing the therapeutic effectiveness and causing harmful side effects on healthy tissues. This is especially concerning in cancer therapy, where traditional chemotherapy drugs fail to selectively target tumors, affecting both cancerous and healthy cells. As a result, high doses are often needed to reach effective concentrations at the target site, increasing the risk of toxicity. Therefore, developing strategies to overcome these challenges and improve targeted drug delivery continues to be a key focus in medicine[1,2].

Methotrexate is a versatile medication employed in cancer and autoimmune disease treatment. It was among the first anticancer agents prescribed for various cancers. Classified as an antimetabolite, Methotrexate inhibits dihydrofolate reductase (DHFR), an enzyme critical for DNA, RNA, and protein synthesis in rapidly dividing cells[3]. Despite its therapeutic efficacy, Methotrexate's clinical use is hindered by rapid tissue release, short half-life, lack of specificity, drug resistance potential, and dosage-related side effects[4,5]. Nevertheless, advancements in delivery technologies present opportunities to

mitigate these limitations and enhance Methotrexate's therapeutic profile, renewing its clinical applicability[6-8].

Targeted drug delivery systems (DDSs) present a complex area of study. DDSs enhance drug half-life, protect against filtration, and reduce side effects[9]. Controlled drug releases are engineered to optimize therapeutic effects while minimizing adverse effects[2]. Numerous innovative systems have emerged as drug delivery mechanisms, with smart control and targeted release into cancerous tissues posing significant challenges in diminishing chemotherapy side effects[10,11].

Consequently, disparities between healthy and cancer cells, such as pH and temperature differences, as well as specific tumor enzymes, are utilized to optimize nanoparticles for selective drug release in tumors. Ideal drug delivery systems are characterized by high drug-loading capacity, superior controlled release, simplicity, and good biocompatibility[12,13].

To achieve optimal drug delivery, carriers, such as nanoparticles have garnered considerable attention due to their ability to prolong drug molecule degradation and enable targeted delivery to pathological tissues [1]. Recent advancements in nanotechnology within pharmaceutical sciences have been remarkable[14].

Many nanoscale materials exhibit hierarchical structures. Nanoparticles, characterized by hierarchical arrangements of atoms or molecules, possess unique properties and functionalities[15]. A hierarchical structure in nanomaterials denotes a multi-level component arrangement crucial for tailoring properties and functionalities for specific uses, including catalysis[16], sensors[17], drug delivery [18], and energy storage[19].

Hierarchically organized systems attract significant research interest due to their distinctive properties and advantages. These porous, stable, and flexible systems with high active surface areas can respond to various external stimuli, making them potentially valuable as drug delivery carriers[20,21].

Noble metal nanostructures have emerged as a favored option among the spectrum of nanocarriers due to their multifaceted advantages[22]. These advantages encompass an exceptionally high surface area, tunable pore diameter and volume, appropriate stability, commendable biocompatibility, and inherent antimicrobial characteristics. Such attributes render them particularly advantageous for the surface-functionalized drug delivery system delivery of anticancer therapeutics[23].

In addition to the aforementioned structures characterized by simplistic geometries, recent advancements in synthesis have unveiled a novel class of complex flower-like or star-shaped morphologies, which include gold stars, nanoflowers composed of palladium, platinum, and gold, as well as starfish-like nanocrystals, among others. These intricate structures generally exhibit a central metallic sphere from which multiple sharp protrusions extend in a tri-dimensional manner[13,24]. In comparison to the flower-like formations of Au [25], Pd [26], Pt [27], and Rh [28], there exists a paucity of literature regarding silver nanoflowers [22].

A recently identified nanostructure of silver, termed “flower-like silver nanostructure,” is characterized by its resemblance to a floral structure, featuring several rod-like extensions radiating outward in three dimensions from a central silver core [28,29]. Notwithstanding their intriguing properties, achieving a high degree of structural anisotropy in noble metal nanoflowers continues to present a formidable challenge [30].

In recent years, hierarchical flower-like iron-doped silver (Ag-Fe) nanostructures have shown great promise in various fields, including oxygen reduction reactions, amperometric detection of hydrogen peroxide, and environmental remediation. For example, in reference 30 studied these nanostructures as electrocatalysts for oxygen reduction reactions, demonstrating enhanced catalytic activity due to their unique morphology and the combination of silver and iron. Similarly, in reference 32 explored iron-doped silver meso-hierarchical flower-like structures for highly efficient nonenzymatic amperometric detection of hydrogen peroxide, highlighting their multifunctionality, including their ability to improve cellular interactions. However, despite these encouraging results, the use of hierarchical flower-like Ag-Fe nanostructures in drug delivery remains underexplored. This study aims to examine their potential in targeted drug delivery and theranostic applications, a promising area of research. The HFAg-Fe nanostructures offer several key advantages for drug delivery, helping to address some of the main challenges in the field. Their large surface area allows for efficient drug loading, while the presence of iron can reduce systemic toxicity and enhance the therapeutic effect by directing drugs specifically to targets like tumors. Additionally, their pH-responsive nature ensures controlled drug release in acidic environments, such as those found in tumors, which allows for more accurate and effective treatment. The silver component also promotes the generation of reactive oxygen species (ROS), enhancing anticancer effects and making these nanostructures particularly promising for theranostic applications. With these unique properties, HFAg-Fe stands out as a versatile and highly effective platform for surface-functionalized drug delivery system drug delivery systems.

Recent research has shown that heteroatom doping is a valuable method for adjusting the physicochemical and biological properties of noble metal nanostructures. Iron doping, in particular, has gained significant attention for its ability to create lattice defects, modify surface chemistry, and introduce redox-active sites. By integrating iron into silver-based hierarchical nanostructures, it becomes possible to control drug loading efficiency, release behavior, and interactions with cells. Additionally, iron-doped silver nanoflowers offer a versatile platform with potential uses in drug delivery, imaging, and redox-based therapies. With this in mind, iron doping was intentionally used in this study to improve the performance of silver nanoflowers as a methotrexate delivery system.

Based on the findings delineated in this study, the synthesis of a hierarchical structure of silver doped with three-dimensional iron (HFAg-Fe) as a drug delivery vehicle and its application in targeted therapeutic delivery are documented. The HFAg-Fe floral structures were synthesized *via* a straightforward and economically viable chemical reduction approach, utilizing malonic acid as a capping agent to modulate the morphology and surface roughness of HFAg-Fe. The incorporation of iron doping can markedly alter the properties and configuration, thereby create additional active sites while preserve the hierarchical architecture [30-32].

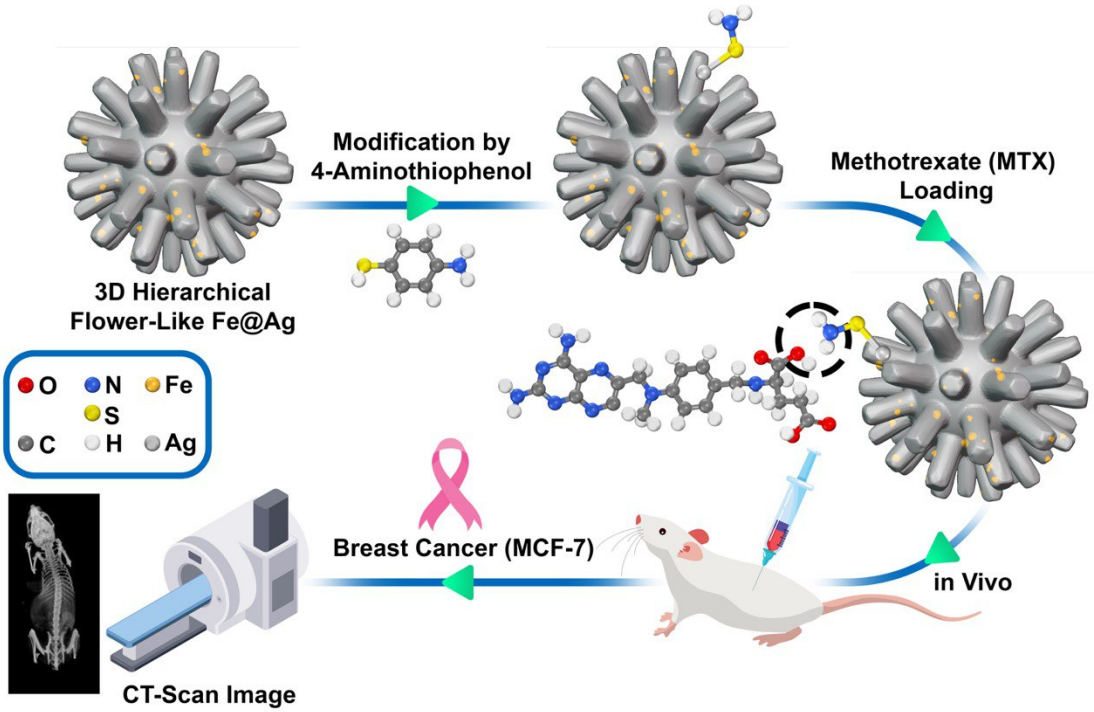

Figure 1. Illustration of 3D flower-like Ag-Fe nanostructures functionalized with 4-aminothiophenol, loaded with Methotrexate (MTX), and evaluated in vivo and vitro against breast cancer (MCF-7)

2. Experimental Section

2.1. Chemicals and instrumentation

All the chemicals used such as silver nitrate, iron(III) nitrate, malonic acid, ascorbic acid, 1-ethyl-3-(3-dimethyl aminopropyl)carbodiimide (EDC), *N*-hydroxysuccinimide (NHS), dimethylformamide (DMF), DAPI (2-(4-Amidinophenyl)-1*H*-indole-6-carboxamidine), isopropanol, FITC (Fluorescein isothiocyanate), PBS (Phosphate Buffer Saline), FBS (Fetal Bovine Serum) purchased from Sigma-Aldrich and Merck chemical companies and were used as received without any further purification. Dialysis membranes (MWCO 8000-14000 Da) were obtained from Mucklin Co. and 96 well plat (sorfa) Drabkin's regent (Baharafshan Instriltute of research & development), standard hemoglobin, L929 Cell lines were purchased from the Iranian Biological

Resource Center (IBRC), MCF-7 cell line was obtained from the Pasteur Institute cell bank in Iran (Tehran, Iran), deionized water (resistivity of 18.2 MΩ cm) prepared by a Milli-Q reagent deionizer (Millipore) was used to prepare all solutions.

2.2. Synthesis of Hierarchical Flower-like Silver and Iron-Doped Structures

The synthesis method strictly follows the procedure outlined in the original paper, with no modifications made to the original method [32]. During this experiment, the effect of the concentration of malonic acid as a structure-directing agent on the morphology of the iron-doped silver nanostructures obtained was investigated. The iron-doped silver nanostructures were prepared using a simple chemical procedure with different concentrations of malonic acid.

To prepare the HFAg-Fe, an aqueous solution of $AgNO_3$ (1 mL, 1 M) was added to varying volumes (0 to 200 µL) of malonic acid solution (0.25 M) in deionized water. The mixture was then left for 10 minutes at 5 °C. Subsequently, an aqueous solution of ascorbic acid (1 mL, 1 M) was added as a reducing agent, and the reaction mixture was vigorously stirred for 15 minutes. The color of the solution changed quickly to gray, which indicated that silver nanoparticles were formed. The same method was used to make iron-doped silver nanostructures. In this manner, different amounts of iron (III) nitrate solution (0.1 M, 50, 100, 150, 200, and 250 µL) were added to a solution of $AgNO_3$ (1 M, 1 mL) and malonic acid (0.25 M, 50 µL) in deionized water (Note: the concentration of the structure directing agent was optimized to create the most active silver flowers). After stirring the mixture vigorously for 10 minutes at 5 °C, the reducing agent (ascorbic acid) was added. The resulting iron-doped

silver structures were precipitated, washed several times with deionized water, and then ready for further use[32].

2.3. Surface modification of hierarchical flower-like Iron-doped silver nanostructures, HFAg-Fe

To prepare the amino-functionalized iron-doped silver nanostructure, HFAg-Fe (100 mg) was suspended in ethanol (10 mL) and stirred for 5 minutes. Then, 4-aminothiophenol (20 mg) was added to this suspension and the mixture was sonicated at room temperature for 20 minutes. At the end, the mixture was left aside for 12 hours. During this period, the mixture was shaken occasionally. Finally, the functionalized iron-doped silver nanostructure was washed with ethanol (3×10 mL) and dried for 1 hour. The HFAg-Fe were made under different pH and temperature conditions for optimization[33].

2.4. Preparation of MTX-loaded hierarchical flower-like Iron-doped silver nanostructure, MTX-HFAg-Fe

MTX was loaded onto HFAg-Fe via both electrostatic and covalent interactions. Before loading the drug, the UV-Vis absorption of free methotrexate (MTX) was measured at 303 nm. The drug loading content was calculated based on the standard curve obtained from the solution of MTX in dimethylformamide (DMF).

To load the MTX drug onto the (HFAg-Fe), a mixture of HFAg-Fe (10 mg) in PBS (10 ml) was sonicated at room temperature for 30 minutes. Then, a solution of methotrexate (10 mg) in DMF (1 ml), and EDC/NHS (10 mg) was added to activate the carboxyl groups on MTX. The suspension was added dropwise to the carrier solution then stirred for 72 hours. The nanoparticles were subsequently rinsed with DMF and water several times to eliminate any unloaded drug. All supernatants containing the unloaded MTX were collected

and the amount of unloaded MTX was measured by its UV absorption at 303 nm[34].

This procedure was repeated in the absence of EDC and NHS in order to load the MTX electrostatically. The drug-loading process was carried out at five different pH levels.

The drug loading content (DLC) was calculated using the following formula:

$$\textit{Drug-loading content (DLC)} = \frac{\text{concentration of drug loaded in carrier}}{\text{concentration of drug used for loading}} \times 100\%$$

2.5. Drug release

The pH-dependent drug release was evaluated through *in vitro* testing using the dialysis membrane method. A dialysis membrane was filled with HFAg-Fe suspension (1 mL, 0.1 M) at three different pH values (7.4, 5.5, and 4.5) PBS, and acetate buffer (0.1 M) at physiological temperature (37 °C). The receiver compartment was filled with PBS (25 mL) and kept at 37 °C under constant magnetic stirring. The receiver compartment (1 mL) was sampled at specific time intervals, and the same volume of fresh PBS was replaced. Subsequently, the concentration of MTX was measured spectrophotometrically. The cumulative percentage of released MTX was then plotted as a function of time (h)[34].

2.6. Cell culture and treatment

Modified Eagles Medium was used for MCF-7 cells at 37 °C under a humidified atmosphere of 5% CO_2. The media were supplemented with 10% FBS, 0.2% sodium bicarbonate ($NaHCO_3$), and 10 mL/L antibiotic solution. In all the experiments culture medium without nanoparticles served as a control.

2.7. Cell cultures and *in vitro* cytotoxicity measurement of MTX-HFAg-Fe

The *in vitro* cytotoxicity of the as-prepared MTX nanoconjugate was evaluated using the MTT assay to assess cell viability. This study employed two cell lines: the L-929 normal mammalian fibroblast cell line and the MCF-7 human breast cancer cell line In accordance with ISO 10993-535, L-929 cells were chosen due to previous studies demonstrating that they provide more distinct and reliable cytotoxicity results compared to other cell lines, thereby offering clearer interpretation of cytotoxic effects [35]. The tests were conducted at the Kia Nano Bio laboratory, which holds an international ISO 17025 accreditation for conducting biocompatibility tests (license No.: NACI/LAB/1523)

The nanoparticles were extracted with cell culture media (RPMI, including 5% fetal bovine serum) at the concentration of 3.2 mg/ml and 1.6 mg/ml at 37 ± 1 ^{o}C for 24 h under aseptic conditions. The extract of latex was used as a positive control, and high-density polyethylene (HDPE) film as a negative control, both freshly prepared at a surface/volume ratio of 3 cm^2/ml.

Cell lines were seeded into a 96-well plate at a concentration of 1×10^4 cells/well. After 24 hours of incubation (5% CO_2, 37 ± 1 °C, > 90% humidity), when the cells had approximately 80% confluency, the sample extract and controls were replaced with the cell medium. The culture medium is used as a blank. The 96-well plate was then incubated for 24 h (5% CO_2, 37 ± 1 °C, > 90% humidity). After 24 h treatment, the cells were evaluated qualitatively under a phase contrast microscope and cytotoxic reactivity was estimated according to the quantitative morphological grading scale shown in Table 1.

Table 1. Qualitative morphological grading of cytotoxicity of extracts.

Grade	Reactivity	Conditions of all cultures

0	None	Discrete intracytoplasmatic granules, no cell lysis, no reduction of cell growth
1	Slight	Not more than 20% of the cells are round, loosely attached, and without intracytoplasmatic granules, or show changes in morphology; occasional lysed cells are present; only slight growth inhibition is observable.
2	Mild	Not more than 50% of the cells are round, devoid of intracytoplasmatic granules, no extensive cell lysis; not more than 50% growth inhibition observable.
3	Moderate	Not more than 70% of the cell layers contain rounded cells or are lysed; cell layers are not completely destroyed, but more than 50% growth inhibition is observable.
4	Severe	Nearly complete or complete destruction of the cell layers.

After the examination of the plates, the culture medium was replaced with 50 µl of the 1mg/ml of MTT solution and incubated for two h in the incubator at 37 ± 1 °C. Then, the MTT solution was decanted, and 100 µl of isopropanol was added to each well. For quantitative measurement, optical density was determined at 540 nm by Gen5 software using a microtiter plate reader (Biotek). To calculate the reduction of viability compared to the blank following equation was used:

$$\%viability = \frac{\text{OD mean sample}}{\text{OD mean blank}} \times 100$$

If viability is reduced to < 70% of the blank, it has a cytotoxic potential.

2.8. Flow cytometry analysis of apoptosis via Annexin V staining

The cell cycle and apoptosis of MTX nanoparticles were studied at the Tehran Preclinical Core Facility (TPCF) at Tehran University of Medical Sciences, using various dilutions in culture media for assessment. Apoptotic cells were screened by staining with propidium iodide (PI) and fluorescein isothiocyanate (FITC) Annexin V (Cat.640914. Biolegend) and MCF-7 cells at a density of 3×10^5 cells/well were plated in a 6 well culture plate and incubated for 24 h.

The cells were treated with MTX- HFAg-Fe with 3.2 mg/ml concentration at different pH for 24 h. At the end of treatment, cells were collected and washed with PBS and resuspended in 500 µL binding buffer having 5 µL of FITC-Annexin V and PI and kept at room temperature in the dark for 15 min. After incubation, each sample was acquired in a flow cytometer (Partec Cyflow, Germany) and analyzed for apoptotic cells [36,37].

2.9. Cell cycle analysis

The DNA content in the cell cycle was analyzed with the help of flow cytometry. The breast cancer cells at a density of 3×10^5 cells/well were seeded in a six-well plate and treated with MTX- HFAg-Fe nanosystems (3.2 mg/ml in pH= 5 and pH= 7) for 24 h. Treatment of MTX at a concentration (of 3.2 mg/ml) has been used as a positive control. After the treatment, the cells were harvested and fixed in 70% ethanol (at −20 °C for 30 min). Cells were further lysed using 1 ml of 0.2% Triton X-100 in PBS at 4 °C for 30 min, and then centrifuged and resuspended in 500 µL of PBS comprising 20 µL RNase (10 mg/mL) for 30 min at 37 °C. Finally, cells were stained using 10 µL PI (1 mg/mL) in 500 µL PBS for 10–15 min at 4 °C and analyzed using flow cytometry.

2.10. FITC labeled HFAg-Fe nanostructures for cellular localization studies

The cell fluorescence imaging to elucidate nanostructures' interactions with cellular components and their localization in the l929 cell line was also studied. The HFAg-Fe nanocarrier was labeled by FITC in aqueous medium at room temperature for 24 h. Extra non-conjugated FITC stain was washed from nanoparticles several times. After cells were cultivated in a six-well plate, the cells were fixed with 4% formaldehyde for 15 min at room temperature, then gently washed three times in PBS. FITC-labeled nanostructures were added to

wells. The l929 nuclei cells were stained with blue fluorescence 4,6-diamidino-2-phenylindole (DAPI). The stained nuclei cells were imaged using a fluorescence microscope at 100X magnification.

2.11. Determination of hemolytic properties

Our assay leverage is a standard practice, ASTM E2524-22, for *in vitro* preclinical analysis of hemolytic properties of nanoparticles. This test method is similar to ASTM F756, with volumes reduced to accommodate nanoparticulate material.

We used our hemolytic assay to analyze various types of nanomaterials, including HFAg-Fe which was made at pH 5, the HFAg-Fe, which was made at pH 7.4, and Methotrexate. Nanoparticulate test samples were prepared at the concentrations of 0.2, 0.4, 0.8, 1.6, and 3.2 mg/ml, diluted in Dulbecco's Phosphate-Buffered Saline (DPBS) with a pH of 7.4[38].

2.11.1. Blood draw

The blood samples were obtained from healthy adult volunteers who provided fully informed and written consent. The experimental protocol for the collection and use of these samples was reviewed and approved by the Institutional Ethics Committee of Kia Nano Bio Lab, an ISO/IEC 17025-accredited biocompatibility testing facility. The approval reference number is NACI/LAB/1523[39].

An equal amount of three donors' whole human blood containing 0.1 M of sodium citrate as an anticoagulant mixed as a pool of blood. The mixture of the collected blood supernatant and CMH reagent at a ratio of 1:1 is used to determine the PFH. The calculated PFH concentration was below 1 mg/ml and suitable for the procedure.

2.11.2. Hemoglobin standard: The standard curve is created from a linear regression with the absorbance values at 540 nm and standard hemoglobin concentrations covering the range from 0.025 mg/ml to 80 mg/ml.

2.11.3. Hemoglobin present and dilution: Total blood hemoglobin (TBH) is determined by adding 20.0 µl pooled blood to 5.0 ml of Drabkin's regent. The absorbance is read on a spectrophotometer at 540 nm.

2.11.4 Procedure of testing material: Pooled whole blood is diluted with DPBS to adjust TBH concentration to 10 mg/ml. 100 µl of each sample, blank (DPBS without sample), negative control (polyethylene in DPBS), and positive control (10% solution of Triton X-100 in DPBS), is added separately to microcentrifuge tubes in replicate. 700 µl of the diluted whole blood was added to each tube. Potential interference of nanomaterial with assay is evaluated using a 100 µl sample and 100 µl of DPBS.

Blood tubes incubated with nanoparticulate material were placed in a water bath set at 37◦C ± 1◦C for three h ± 15 min, mixing the sample by rotation every 30 min. Then, the tubes were centrifuged for 15 min at 800g. Each supernatant was combined with Drabkin's reagent at a ratio of 1:1, and 100 µl of the mixture was filled in each well of the 96-well plate by replicate. The absorbance was read at 540 nm to determine the concentration of hemoglobin[38].

The percent hemolysis was calculated by correcting for the background from the blank sample:

$$\text{Blank corrected \% hemolysis} = \frac{\text{S-B}}{\text{(T/8)-B}} \times 100\%$$

The results of the test sample compared to the results of the negative control, using the Table 2 as a guide:

Table 2. A % hemolysis >5% indicates that the test material will cause damage to red blood cells.

Hemolytic index (%)	Hemolytic grade
0-2	Nonhemolytic
2-5	Slight hemolytic
˃5	Hemolytic

2.12. X-ray Micro-Computed Tomography

In this study, we used an *in vivo* X-ray Micro-Computed Tomography (micro-CT) scanner (LOTUS *in vivo*, Behin Negareh Co., Tehran, Iran) at the Tehran Preclinical Core Facility (TPCF) based at Tehran University of Medical Sciences. All experimental protocols involving animals were approved by the Ethics Committee of University of Isfahan IR.UI.REC.1403.087. All methods were carried out in accordance with the relevant guidelines and regulations, and the study was conducted and reported in compliance with the ARRIVE guidelines. In order to obtain the best possible image quality, the X-ray tube voltage and its current were set to 70 kV and 100 µA, respectively, and the frame exposure time was set to 1 second by 1.4 magnification. The total scan follow up was 14 days. Slice thicknesses of reconstructed images were set to 30 micrometers. All the protocol settings were controlled by LOTUS-in vivo-ACQ software. The acquired 3D data was reconstructed using LOTUS *in vivo*-REC by a standard Feldkamp, Davis, Kress (FDK) algorithm. Also, LOTUS NDT-3D was used for rendering reconstructed images.

2.13. Histological study

At the end of the experimental period, Prior to euthanasia, animals were anesthetized using ketamine (80 mg/kg) and xylazine (10 mg/kg) administered intraperitoneally. After confirming deep anesthesia, euthanasia was performed by CO_2 inhalation in accordance with institutional and international ethical guidelines. Animals were sacrificed by gradual exposure to carbon dioxide in a closed chamber at a rate of approximately 20–30% of the chamber volume per minute to ensure a smooth and painless loss of consciousness, following the ethical standards approved by the ISO 10993-2 requirements for animal welfare. After the complete cessation of respiration and heartbeat, cervical dislocation was performed as a secondary physical method to confirm death. The euthanasia procedure was carried out in accordance with the AVMA Guidelines for the Euthanasia of Animals (2020) and followed the ethical standards approved by the ISO 10993-2 requirements for animal welfare.

The liver and spleen were excised, washed with saline, and fixed in 10% formalin for 24-48 hours. After fixation, the tissues were dehydrated, cleared in xylene, and embedded in paraffin. Sections (4–5 µm thick) were prepared and stained with hematoxylin and eosin (H&E) for histological evaluation. The stained slides were examined under a light microscope at ×100 and ×400 magnifications. Histopathological changes such as degeneration and necrosis were assessed by a blinded histopathologist [40].

Tumor tissues were collected from breast cancer bearing mice at days 1, 7, and 14 post-treatment. Samples were fixed in 10% neutral buffered formalin for 24 h, dehydrated through a graded ethanol series, cleared in xylene, and embedded in paraffin.

Paraffin-embedded tumor blocks were sectioned into 4–5 µm thick slices, mounted on glass slides, and subjected to hematoxylin and eosin (H&E) staining following the ethical standards approved by the ISO 10993-2 requirements for animal welfare. Histological examination was performed to assess tumor morphology, cellular integrity, necrosis, and the presence of localized dense deposits associated with the accumulation of nanostructure-based formulations. Stained sections were examined using an optical microscope, and representative images were captured at 100× magnification

3. Results and discussion

3.1. Preparation of 3D hierarchical flower-like iron-doped silver nanostructures, HFAg-Fe, and nanocarrier

Hierarchical iron-doped silver nanostructures with various unique flower-like morphologies have been successfully prepared *via* a simple chemical procedure (Figure 2). For this purpose, a solution of iron(III) nitrate was added to a solution of $AgNO_3$ and malonic acid following by addition of ascorbic acid as reducing agent.

To load the MTX on the carrier, the surface of HFAg-Fe was first modified by using a self-assembly reaction to coat the silver surface with 4-aminothiophenol. This method was chosen due to the silver surface's tendency to bond with the thiol functional group of 4-aminothiophenol. The interaction is based on the interaction of acids with soft and hard bases. The thiol group acts as a soft Lewis base for silver (the acid), resulting in modified Flower-like silver surfaces.

The amount of sulfur in the structure was measured using elemental analysis (CHNS analysis), yielding about 3.5%, which confirms the successful attachment of 4-aminothiophenol on the silver surface (Figure 2).

It should be emphasized that 4-aminothiophenol does not possess any intrinsic targeting capability. In this study, it is employed exclusively as a bifunctional linker to achieve stable drug conjugation on the surface of the silver nanostructures. The thiol (–SH) moiety exhibits strong chemisorption onto the silver surface through the formation of Ag–S bonds, providing robust anchoring of the linker. Subsequently, the exposed amine ($–NH_2$) group reacts with the carboxyl group of methotrexates via EDC/NHS-mediated coupling, leading to the formation of a covalent amide bond. This conjugation strategy enhances drug loading stability and prevents premature drug release, but does not confer any active or receptor-mediated targeting ability. Consequently, the accumulation of the nanostructures in tumor tissue is primarily governed by passive targeting through the enhanced permeability and retention (EPR) effect.

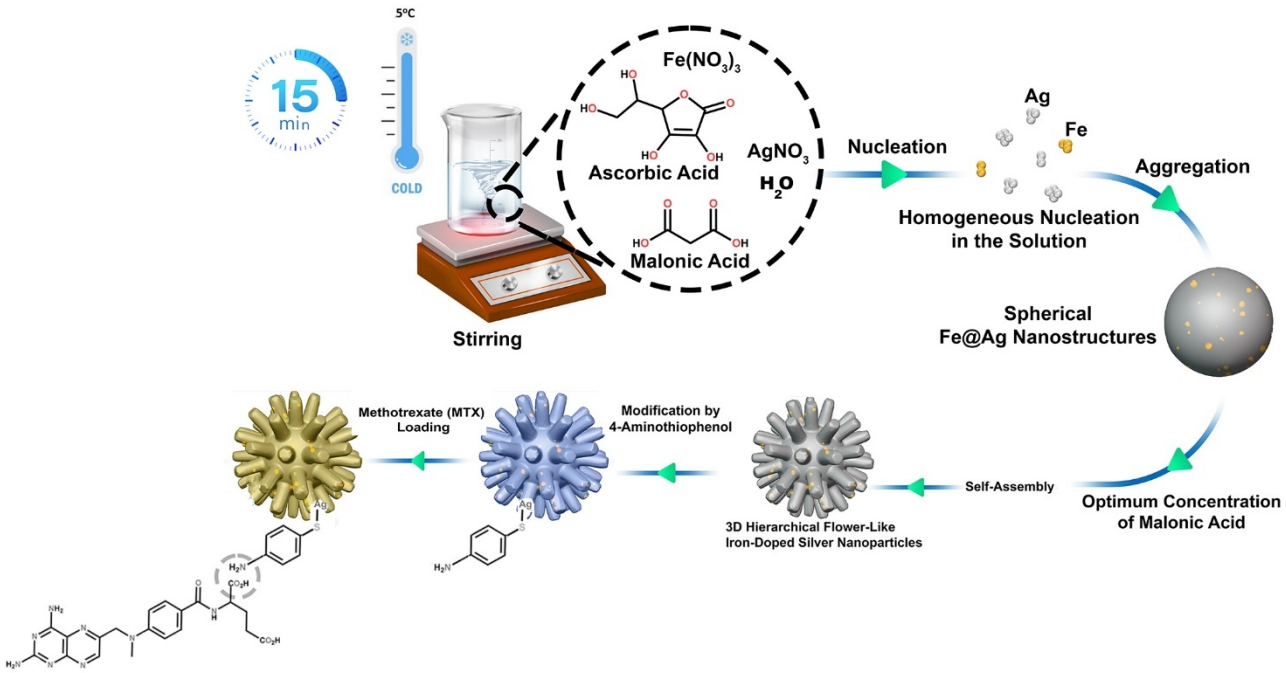

Figure 2. Illustration of HFAg-Fe preparation process and loading of MTX drug on it.

3.2. Characterization of HFAg-Fe, nanocarrier and drug delivery nanosystem

The surface morphology and structure of obtained flower like silver were studied by FE-SEM and AFM.

As shown in Figure 3a-c, the concentration of the directing agent has a significant effect on the morphology of the obtained silver particles. Without using malonic acid, silver particles bearing ball-like structures (~1 µm diameter) were observed (Figure 3a), while in the presence of dilute malonic acid (~0.5 mM), small buds with ~90 nm average particle size were produced. The formation of these buds progressed with an increase in malonic acid concentration. Specifically, the addition of 1 mM malonic acid resulted in the development of silver particles exhibiting a chrysanthemum flower-like

structure. These structures were composed of intersecting sheets, with an average particle size of approximately 72 nm (Figure 3).

The morphology of iron-doped silver nanostructures is primarily controlled by the concentration of malonic acid. At low concentrations, weak surface stabilization leads to isotropic growth, whereas higher concentrations promote selective carboxylate adsorption on specific silver facets, suppressing their growth and inducing anisotropic, flower-like structures. Concurrent Ag^+ complexation modulates reduction kinetics, enabling hierarchical self-assembly. Iron incorporation further stabilizes reactive facets without altering the overall growth mechanism.

Figure 4 demonstrates that doping silver with low iron content (0.2 mM iron ions) results in iron-doped silver particles with a flower-like structure. These particles are made up of loosely packed silver nanosheets with an average size of about 50 nm, providing a surface area approximately four times greater than that of ball-like silver particles. This unique structure offers the best performance for drug loading and release. Doping iron atoms and creating distinct structures is seen as a practical method to design highly active surfaces and enhance the surface area to expose more active sites for drug loading [41].

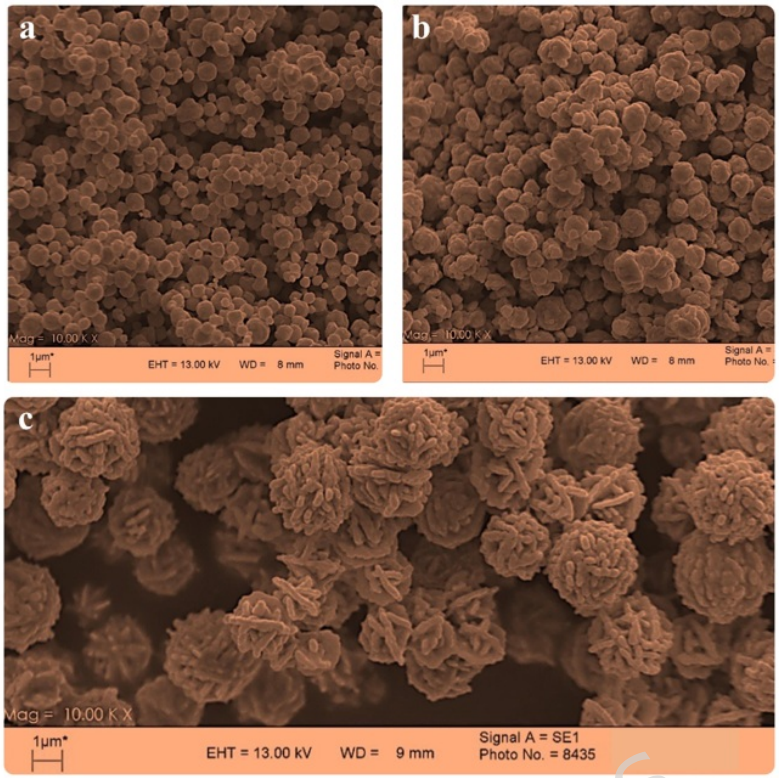

Figure 3. SEM images of hierarchical flower like Iron doped silver nanostructures (HFAg-Fe) prepared: (a) in the absence of malonic acid and in the presence of (b) 0.5 mM, malonic acid (c) 0.5 mM, malonic acid, 0.2 mM iron (III) nitrate

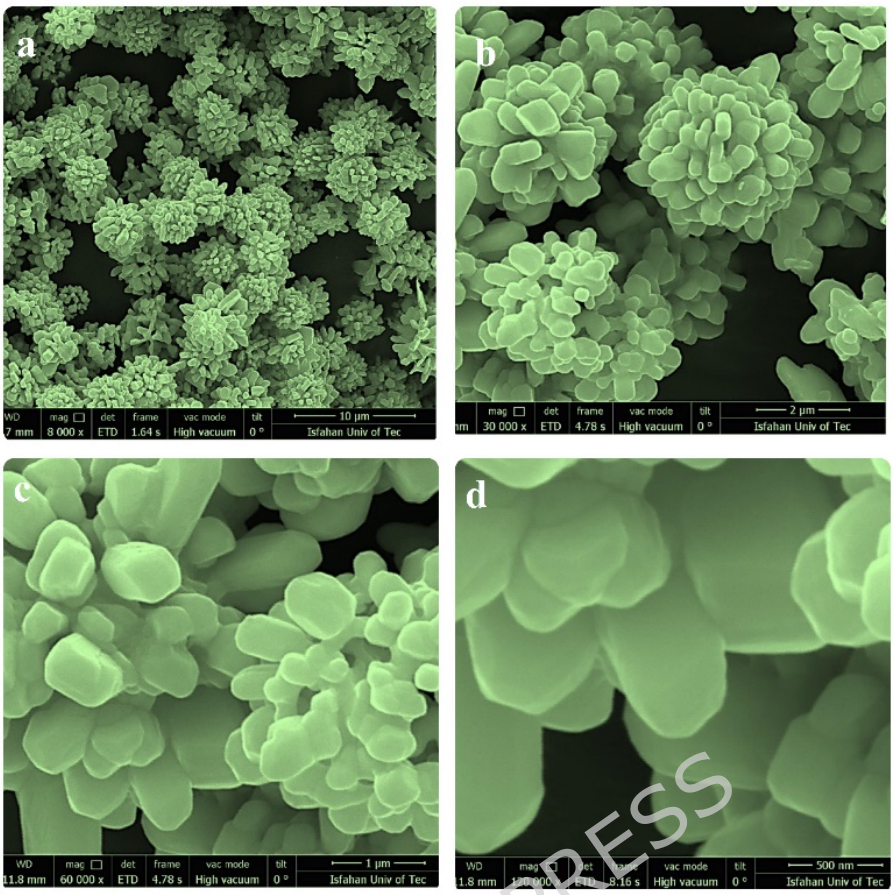

Figure 4. SEM images of HFAg-Fe prepared by 0.5 mM, malonic acid, 0.2 mM Fe(III) nitrate before Methotrexate loading

Figure 5 shows the SEM images of HFAg-Fe which the MTX drug has been loaded on it *via* an amide linkage (The loading process will be fully discussed in the next section). As observed, the methotrexate molecules are successfully attached to the surface of the flower-like structure and during this process, the carrier structure remains intact.

Energy-dispersive X-ray spectroscopy (EDS) was employed to analyze the bulk compositions of the HFAg-Fe flowers (Figure 6). The inset of Figure 6 provides EDS mapping of HFAg-Fe flowers, confirming the successful incorporation and uniform distribution of iron throughout the silver flower nanostructure. The

EDS elemental distribution across the selected area further validates the homogeneous dispersion of iron within the silver matrix [42].

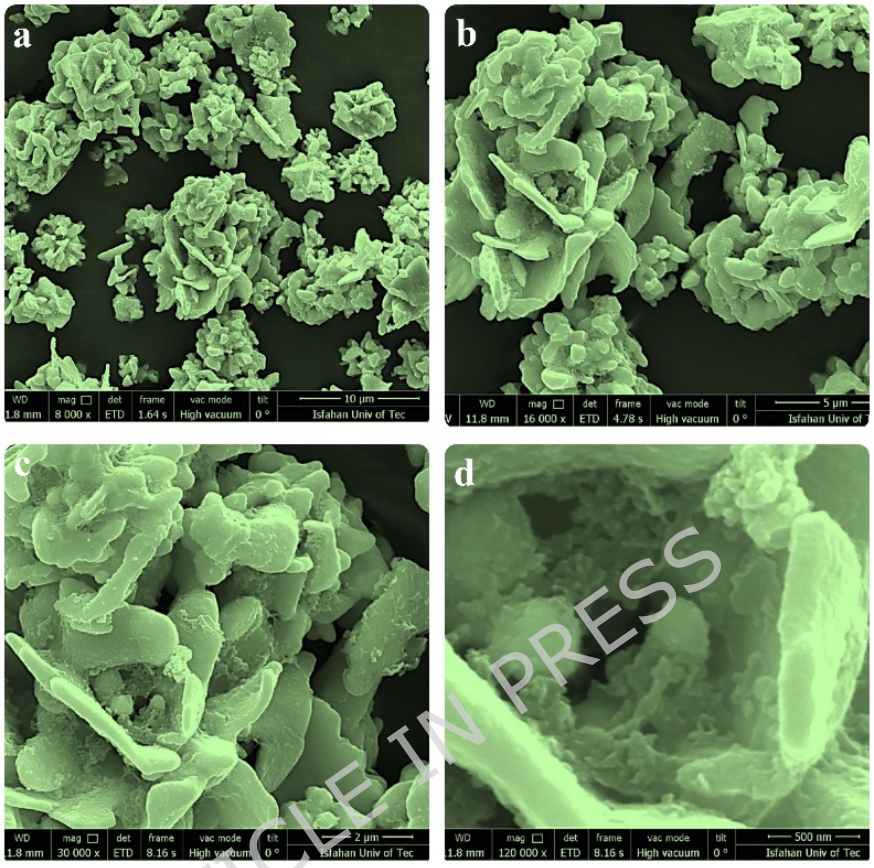

Figure 5. SEM images of hierarchical flower-like iron-doped silver nanostructures loaded with Methotrexate at different magnifications. (a) Low magnification image (8000x), showing the overall structure of the nanostructures. (b) Medium magnification image (16000x), highlighting the flower-like morphology. (c) High magnification image (30000x), showing the detailed surface structure. (d) Ultra-high magnification image (120000x), revealing the fine features of the individual nanostructures.

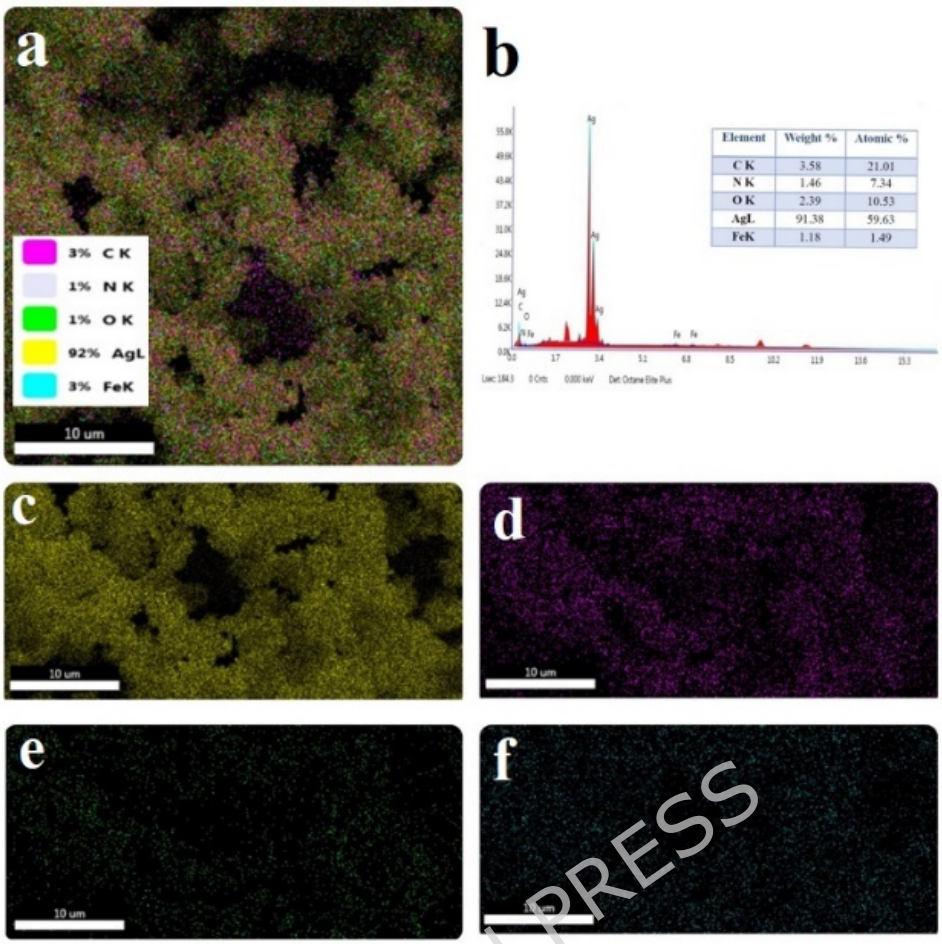

Figure 6 (a, c, d, e, f) EDX elemental mapping image of HFAg-Fe (b) EDX spectrum of HFAg-Fe. four constituents over the selected area (Ag, Fe, C, O)

AFM was used to obtain further details of the surface topology such as thickness and roughness over an area of 1000 nm × 1000 nm. The 2D and 3D AFM images (Figure 7a and b) of the sample show hill and valley like for HFAg-Fe. The root mean square (rms) roughness is about 3.086 nm and the average roughness is 2.434 nm in the 1.215 nm × 1.215 nm scan area [43].

The roughness histogram showed a Gaussian like distribution for the HFAg-Fe structure (Figure 7c).

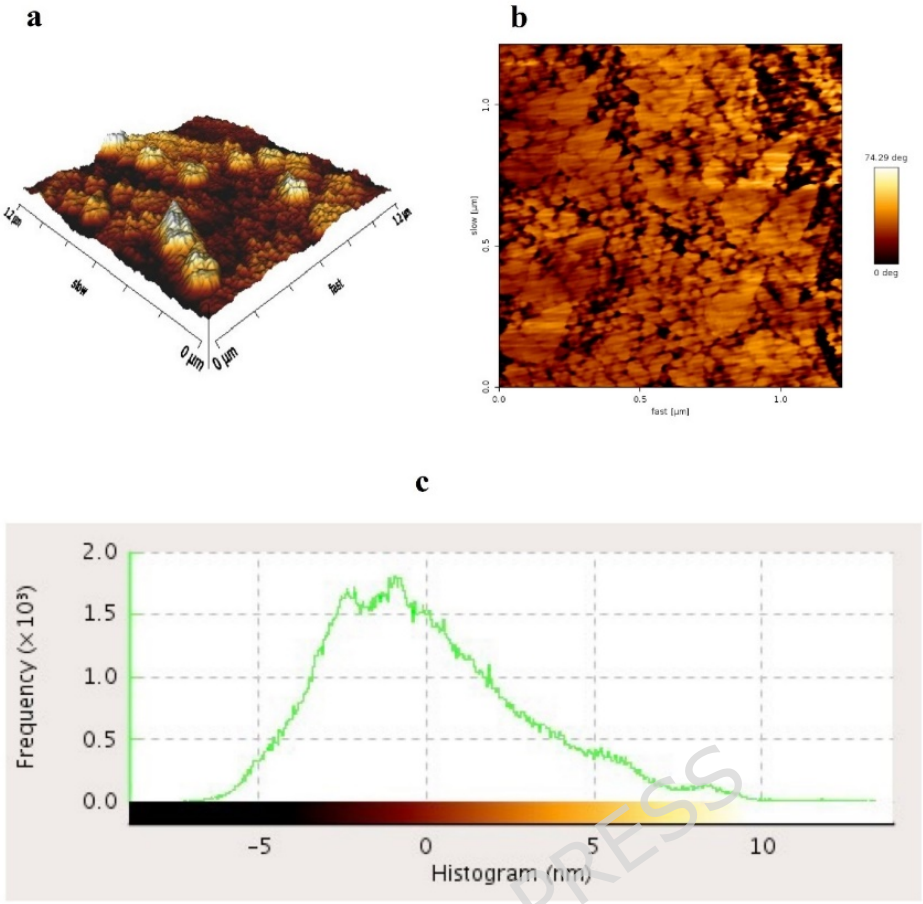

Figure 7. AFM image showing the surface morphology for HFAg-Fe

Moreover, the crystallinity of the as-prepared HFAg-Fe nanostructures was further investigated by XRD. As shown in Figure 8, the XRD patterns for synthesized HFAg-Fenanostructures showed five main characteristic diffraction peaks at 2θ = 38.4, 44.5, 64.8 and 77.7° correspond to (111), (200), (220) and (311) crystallographic planes of face-centered cubic (FCC) Ag crystals [24,44].

The XRD pattern of the HFAg-Fe nanostructure showed five sharp peaks at 2θ= 37.9, 44.1, 64.1, 76.9, and 81.3°, indicating its crystalline nature and correspond to (111), (200), (220), (311) and (222) crystallographic planes of face-centered cubic (FCC) iron-doped silver crystals.

XRD analysis of HFAg-Fe/MTX showed a substitution pattern from sharp peaks of the drug to broad peaks, which suggests that the drug is dispersed in an amorphous form in the hierarchical flower like iron-doped silver matrix. This patterns also confirms the successful loading of methotrexate onto the HFAg-Fe and indicate the uniform and homogeneous distribution of the drug within the nanostructures and preservation of the crystalline properties of silver and iron after drug loading [45].

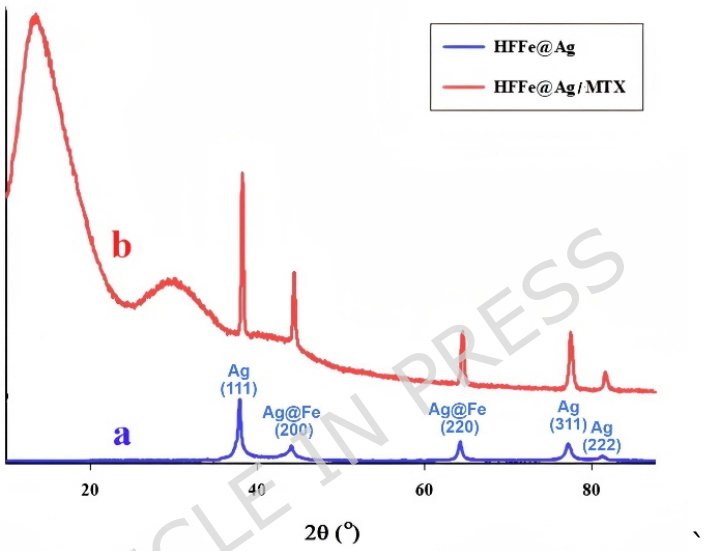

Figure 8. XRD patterns of hierarchical flower like (a) HFAg-Fe and (b) HFAg-Fe /MTX.

Further structural information was obtained by FT-IR spectroscopy. In the FT-IR spectrum of HFAg-Fe, the band at the 3427 cm^{-1} corresponds to stretching vibrations of hydroxy groups (O–H). The band at 2926 cm^{-1} corresponds to the stretching vibrations of aliphatic C–H bonds (Figure 9a).

The vibrational bands typically found in the low-frequency region (400-600 cm^{-1}) indicate the presence of silver and iron oxides.

When HFAg-Fe was modified with 4-aminothiophenol (4-ATP), the FT-IR spectrum (Figure 9b) reflected the vibrational modes of both the metal-doped

nanoparticles and the surface-bound 4-ATP. The band around 3441 cm^{-1} for the amine group (-NH_2) of 4-aminothiophenol, the band at 1629 cm^{-1}, corresponding to the (N-H) bending vibrations of the amine group and the Following the attachemnt of thiol groups of 4-aminothiophenol to the surface of HFAg-Fe, the vibrational band corresponding to the S−H bond at 2600 cm^{-1} was not observed, indicating the attachment of a thiol group to the metal surface confirming the successful modification of the HFAg-Fe with 4-aminothiophenol.

The FT-IR spectrum of free methotrexate (Figure 9c) shows a range of characteristic bands including a broad band at 3393 cm^{-1} (O–H stretching vibration of carboxyl groups superposed), a sharp band corresponding to N–H stretching vibration of primary amine at 1643cm^{-1},and C=C stretching from aromatic rings at 1600 cm^{-1} [46]

When MTX is loaded on HFAg-Fe, an amide bond is formed between methotrexate (MTX) and an amine group on a the HFAg-Fe. In the FT-IR spectrum of HFAg-Fe/MTX, the bands corresponding to N-H bending from the amidic group appear in the range of 1500–1600 cm^{-1}, partly overlapping with the aromatic C=C stretching vibrations of the MTX (Figure 9d) [47].

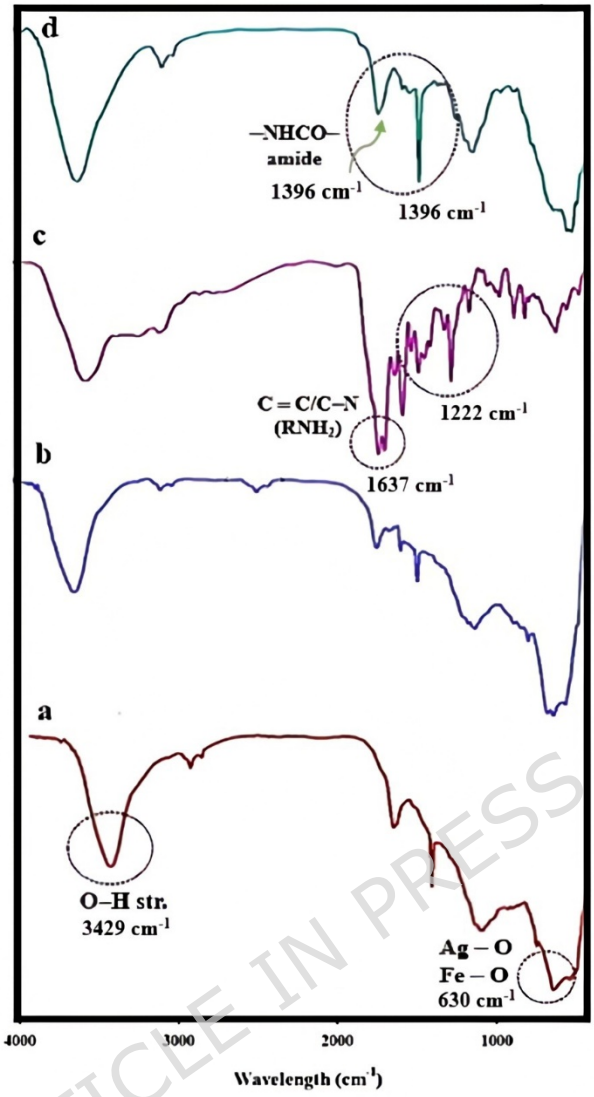

Figure 9. FT-IR spectrum of: (a) HFAg-Fe, (b) HFAg-Fe/NH_2, (c) pure MTX, (d) HFAg-Fe/NH_2/MTX.

3.3. *in vitro* Studies

3.3.1. MTX loading and release profiles

The loading of methotrexate (MTX) onto the HFAg-Fe was achieved using both physical and chemical methods. In the first approach, MTX was loaded onto the HFAg-Fe solely *via* electrostatic interactions between amine and carboxylic acid groups. In the second approach, MTX was loaded onto the HFAg-Fe in the presence of 1-ethyl-3-(3-dimethylaminopropyl)carbodiimide, EDC, and *N*-hydroxysuccinimide, NHS, facilitating covalent bonding through amide bond

formation between the carboxyl groups of MTX and amine groups on the HFAg-Fe (Figure 10). Additionally, the loading potential of HFAg-Fe depends on the type of drug and loading conditions. Moreover, the HFAg-Fe nanostructure contains amino groups, making it an excellent host for drug molecules. Consequently, the optimization of MTX loading was initially conducted as a function of pH. Then, the loading capacity was determined by UV-Vis spectroscopy based on the original MTX solution and the supernatant solution after loading at different pH. As can be seen in Figure 11a, the highest loading of MTX in the absence of EDC and NHS was 26.61% at pH= 5. Given that MTX is a weak acid with multiple pK_a values, its ionization state is prominent in acidic pH. At pH= 5, the carboxylic acid of MTX becomes ionized and interacts with the NH_4^+ groups of the modified HFAg-Fe, leading to a balanced mix of electrostatic and hydrophobic interactions. At lower pH values, the higher ionization rate does not lead to increased drug loading on the carrier. This is attributed to the heightened repulsion between the amine groups of the carrier. The repulsion between the amine groups in the hierarchical flower-like structure can significantly impact the drug loading. The positively charged amine groups, especially at specific pH levels, can create electrostatic repulsion, thereby reducing the available space for drug adsorption and decreasing the overall drug-loading capacity.

As can be seen in Figure 11b, the amount of drug loading on carrier in the presence of EDC and NHS at pH 6 was 9.757 $mg.mg^{-1}$. In this case, an amide bond between carboxyl groups on MTX and amine groups on the carrier is formed [48]. The higher drug loading at pH= 6 is attributed to the presence of EDC and NHS. The EDC activates the carboxyl groups on MTX to form an *o*-acylisourea intermediate. The NHS reacts with the intermediate to form a more

stable NHS ester, which is more reactive towards nucleophiles. The NHS ester then reacts with the amine groups on the HFAg-Fe/NH_2, forming a stable amide bond and effectively conjugating MTX to the HFAg-Fe/NH_2 (Figure 10) [49].

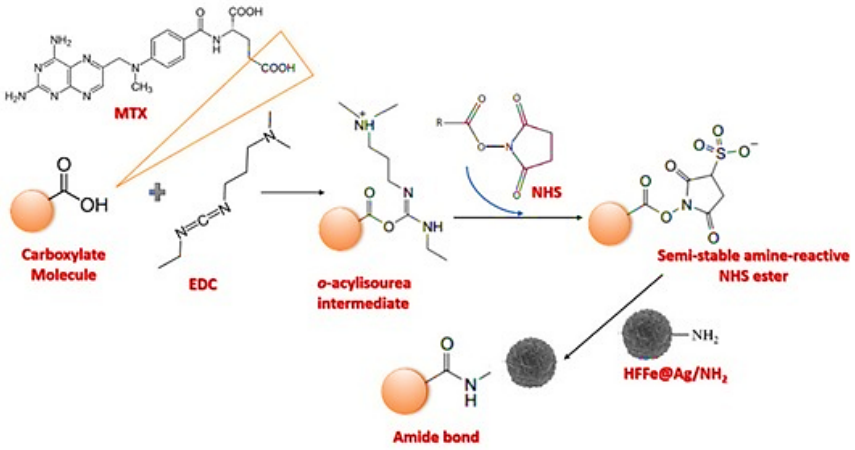

Figure 10. EDC and NHS activation mechanism for attachment of MTX onto HFAg-Fe/NH_2

At pH 7 and 8, the primary amine groups (R-NH_2) are partially protonated to form R-NH_3^+ (they are not fully protonated) because the buffer's pH is lower than the pKa of the amine group. Therefore, the drug loading is lower in this pH.

Due to the higher drug loading the carrier prepared via second approach, all studies were carried out with it.

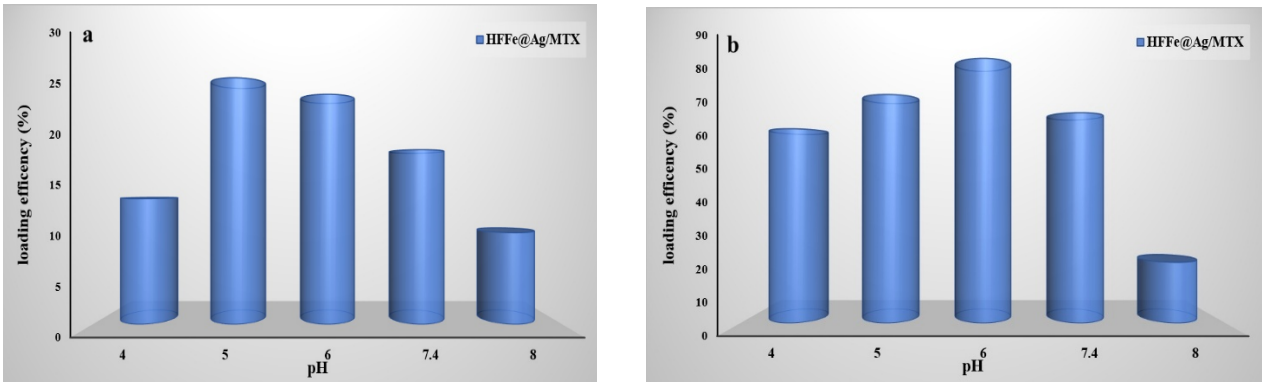

Figure 11. The loading capacity of MTX on HFAg-Fe at different pH values (a) without EDC and NHS (b) in the presence of EDC and NHS.

The *in vitro* release profiles of MTX from HFAg-Fe was investigated in phosphate-buffered saline (PBS) with pH 5.5 (the cancer cells' endosomal pH), 4.5, and 7.4 (the physiological pH) to evaluate how pH variation affects the release of drug from nanocarrier. The release of the drug is associated with the cleavage of the amide bond between MTX and HFAg-Fe.

The cleavage of amide bonds is typically accelerated under acidic conditions. Under physiological conditions (pH 7.4), this cleavage occurs slowly and generally requires enzymatic activity [50,51].

Figure 12 shows the release amount of MTX as a function of time under different pH conditions. The release studies were continued up to 72 h. The results presented in Figure 12c show an apparent pH effect, with a faster release at pH 5.5 (56% after 60 h) and 69% at pH 4.5 compared with the 35% at pH 7.4.

Even though the drug release is higher at pH 4.5, it is not ideal for the drug to be released rapidly in a short period. The intended goal is to achieve a slow and continuous release. At pH 5.5, a constant and uniform plasma concentration of drugs for a specific duration is observes, preventing the fluctuations typical of systemic drug administration. In addition, the pH of breast cancer cells (MCF-7) is between 5 and 5.5.

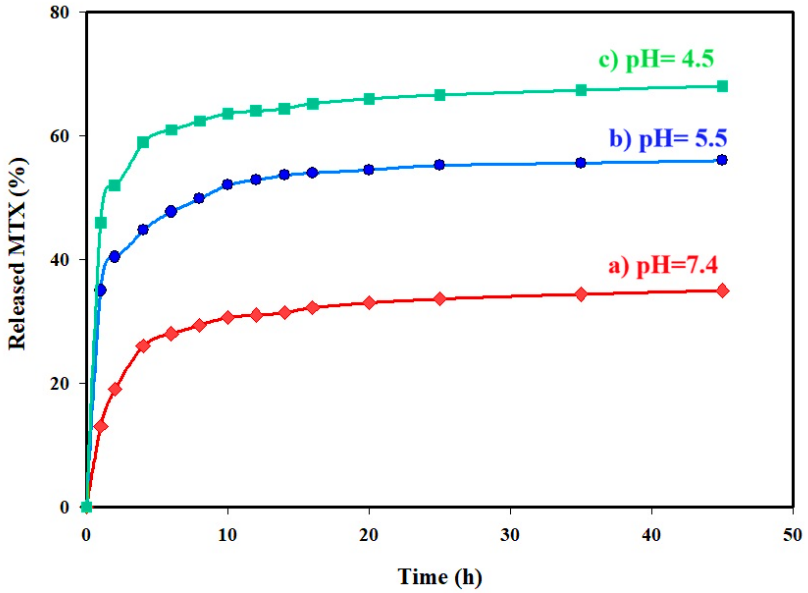

Figure 12. *in vitro* MTX release for HFAg-Fe: (a) pH 7.4 (b) pH5.5 and (c) pH 4.5.

3.4. Biocompatibility of drug delivery system

3.4.1. Cytotoxicity Assay

To measure cell viability or cytotoxicity, we can use the MTT assay, which quantifies mitochondrial succinate dehydrogenase activity in metabolically active cells. This assay is based on the reduction of 3-(4,5-dimethylthiazol-2-yl)-2,5-diphenyltetrazolium bromide (MTT) reagent to formazan, an insoluble purple-colored product, by cellular mitochondrial dehydrogenase. The amount of formazan dye produced is directly related to the number of viable cells. After obtaining the results, they were compared to control cells, and cell viability was calculated using the following formula:

$$\textit{Cell Viability (\%)} = \frac{\text{Absorbance of Treated Sample}}{\text{Absorbance of Control Sample}} \times 100$$

In the cell viability studies, the cytotoxicity of HFAg-Fe, HFAg-Fe/MTX and free MTX were compared to evaluate the efficacy of surface-functionalized drug

delivery system drug delivery. To this purpose, L-929 and MCF-7 were incubated for 24 h.

Microscopic showed that cultures treated with the HFAg-Fe and HFAg-Fe/MTX which was prepared at different pH exhibited no cytotoxic response on L-929 (grade 0), and slight cytotoxic response on MCF-7 (grade 1). Whereas the cells treated with free MTX and positive control showed mild (grade 2) and severe cytotoxicity (grade 4), respectively.

Quantitate analysis of cytotoxicity for the sample is presented in Figure 13. L929 cells treated with HFAg-Fe and HFAg-Fe/MTX exhibited viability greater than 70% (ranging from 70.780 to 97.609%) indicating that the material is non-cytotoxic to L-929 cells. Notable, the cytotoxicity on the MCF-7 cancer cell line was higher compared to the L-929 normal cell line, which is advantageous as it suggests selective toxicity toward cancer cells with minimal effects on normal cells.

The HFAg-Fe/MTX sample prepared at pH= 7 demonstrated superior efficacy compared to other samples, due to the appropriate pH for cell growth. The samples show lower efficacy compared to the pure MTX because the drug loading per unit of HFAg-Fe is lower than the amount of free drug used in the assay.

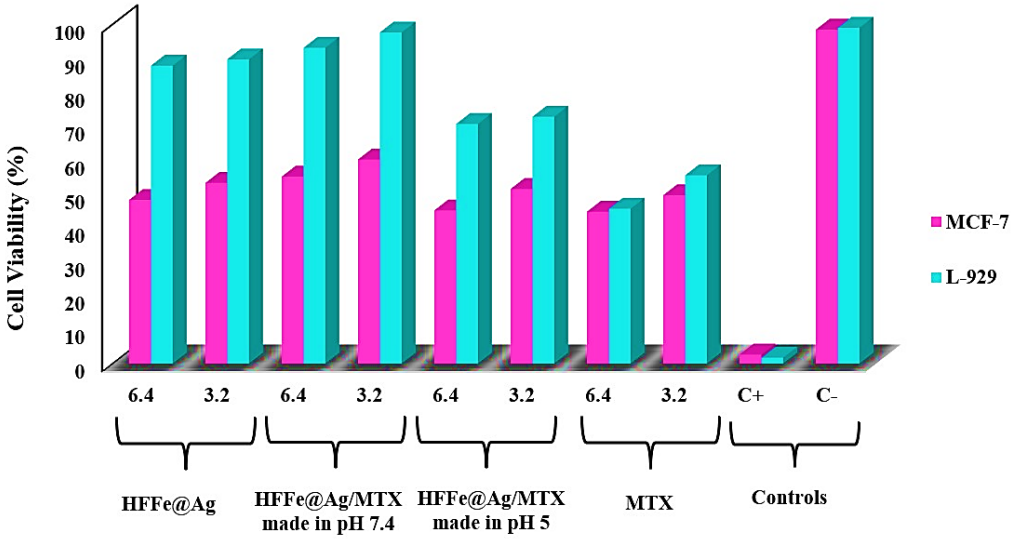

Figure 13. Effect of different concentrations of HFAg-Fe, HFAg-Fe/MTX (pH= 7), HFAg-Fe/MTX (pH= 6), and free MTX MTT on the viability of MCF-7, and L-929 cells, measured by MTT assay.

3.4.2. Flow cytometry analysis

The observed difference in MTX release rates at pH= 5 and pH= 7 indicates the pH-sensitive nature of the nanocarrier (HFAg-Fe) (Figure 14). This property could potentially be harnessed for targeted drug delivery applications, offering controlled release profiles in different physiological environments.

The higher apoptosis rate in MCF-7 cells at pH= 5 compared to pH= 7 suggests that the released MTX is more effective at inducing programmed cell death under acidic conditions. This highlights the importance of considering the tumor microenvironment's pH in developing surface-functionalized drug delivery system therapies for cancer treatment.

Cell cycle analysis revealing cell cycle arrest at the S phase and a significant decrease in G2-M phase further supports the control release effects of MTX on MCF-7 cells (Figure 15). This finding suggests that MTX treatment interferes

with DNA synthesis and cell proliferation, leading to cell cycle arrest and ultimately apoptosis.

Overall, these results provide valuable insights into the potential of pH-responsive nanocarrier (HFAg-Fe) for precise drug delivery and the mechanistic understanding of MTX's effects on MCF-7 cells.

Although HFAg-Fe/MTX exhibits a higher MTX release rate under acidic conditions (pH = 5), this does not directly translate into a stronger apoptotic response compared to free MTX. This discrepancy can be attributed to differences in cellular uptake and intracellular drug availability. Free MTX readily diffuses into cells and rapidly reaches its cytosolic and nuclear targets, whereas HFAg-FeH/MTX is mainly internalized via endocytic pathways. Consequently, part of the released MTX may remain transiently confined within endosomal/lysosomal compartments, limiting its immediate bioavailability. Flow cytometry analysis confirms a higher apoptotic population at pH = 5 than at pH = 7, highlighting the pH-responsive behavior of the HFAg-Fe nanocarrier and its enhanced activity under tumor-like acidic conditions. This finding is consistent with previous reports on pH-sensitive MTX delivery systems, in which acidic environments promote drug release and subsequent apoptotic signaling. However, compared with free MTX, the nanocarrier provides a controlled and sustained release profile, which may lead to a delayed rather than an immediate apoptotic response. Cell cycle analysis further supports this mechanism, as HFAg-Fe/MTX treatment induced pronounced S-phase arrest accompanied by a reduction in the G2/M population. This behavior aligns with the well-known mechanism of MTX through dihydrofolate reductase (DHFR) inhibition and disruption of DNA synthesis. Overall, these results indicate that while free MTX triggers rapid apoptosis, HFAg-Fe/MTX exerts its anticancer

effect via pH-triggered, controlled drug release, resulting in effective cell cycle arrest and regulated apoptosis. Such controlled behavior is advantageous for minimizing nonspecific toxicity while maintaining therapeutic efficacy [4,52].

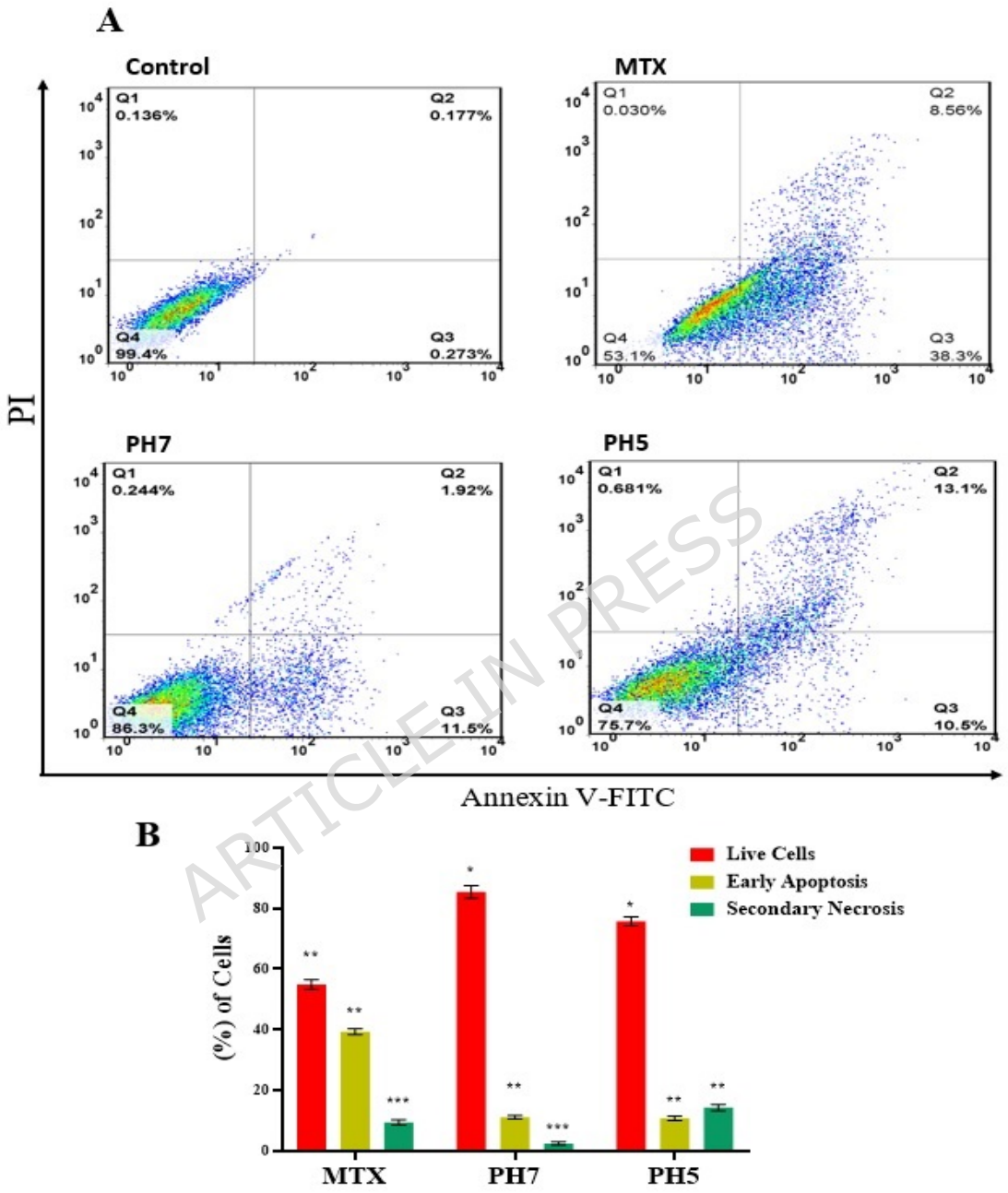

Figure 14. The effect of MTX-Nanoparticles on the cell death in MCF-7 cells evaluated by flow cytometry (A). The percentages of live cells, early and secondary necrotic cells after 24 h post treatment (B). Data are expressed as mean ± SD with n = 3. *p < 0.05, ** p < 0.01, *** p < 0.001 significantly different from control cells.

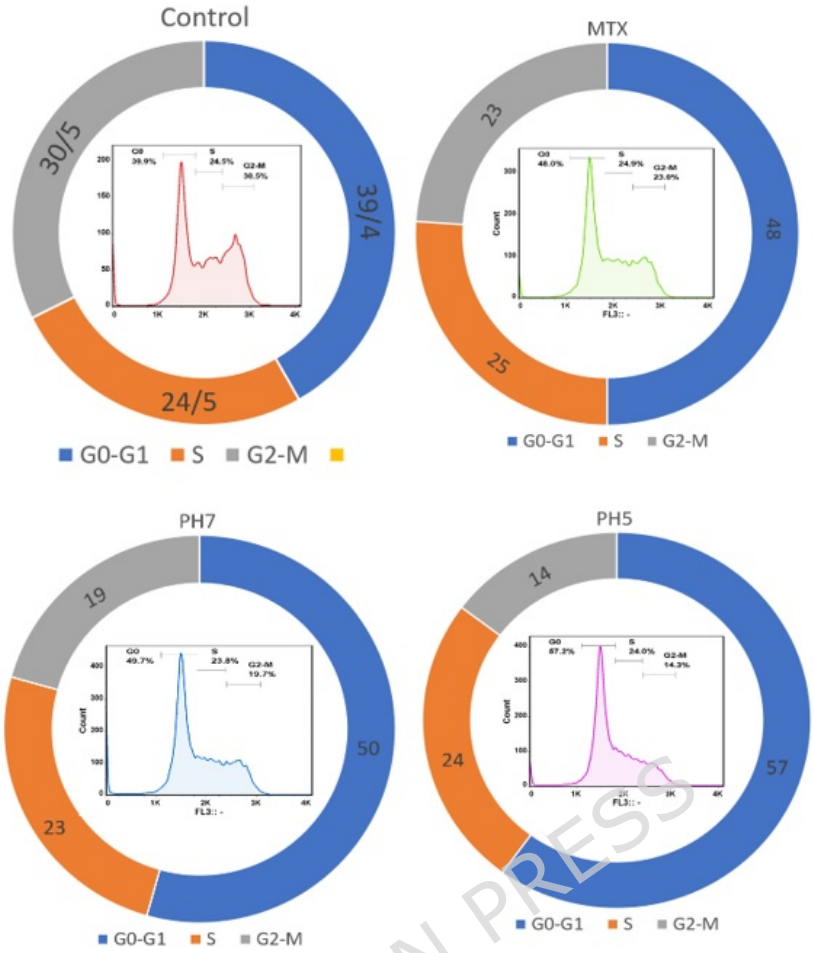

Figure 15. Cell cycle distribution for MCF-7 cells post-treatment with different samples in different pH by flow cytometry. The control sample have not been treated with any drugs or nanomaterials.

3.4.3. FITC labeled hierarchical flower-like iron doped silver for cellular localization studies

The labeled cells were treated with different pH of loading for HFAg-Fe/MTX (5 and 7.4) for 24 h at room temperature. The HFAg-Fe/MTX accumulation and DAPI nuclei staining showed green and blue fluorescence. As shown in Figure 16, images of the DAPI and FITC signals approved the cellular internalization of HFAg-Fe/MTX within L-929 cells after incubation time. These findings indicate that the nanoparticles were able to enter the cell nucleus and bind to DNA, thus achieving the anticancer effect of MTX. It appears that the drug-

delivery systems are sufficiently stable to escape from the endosomes and reach the nucleus for drug release and distribution.

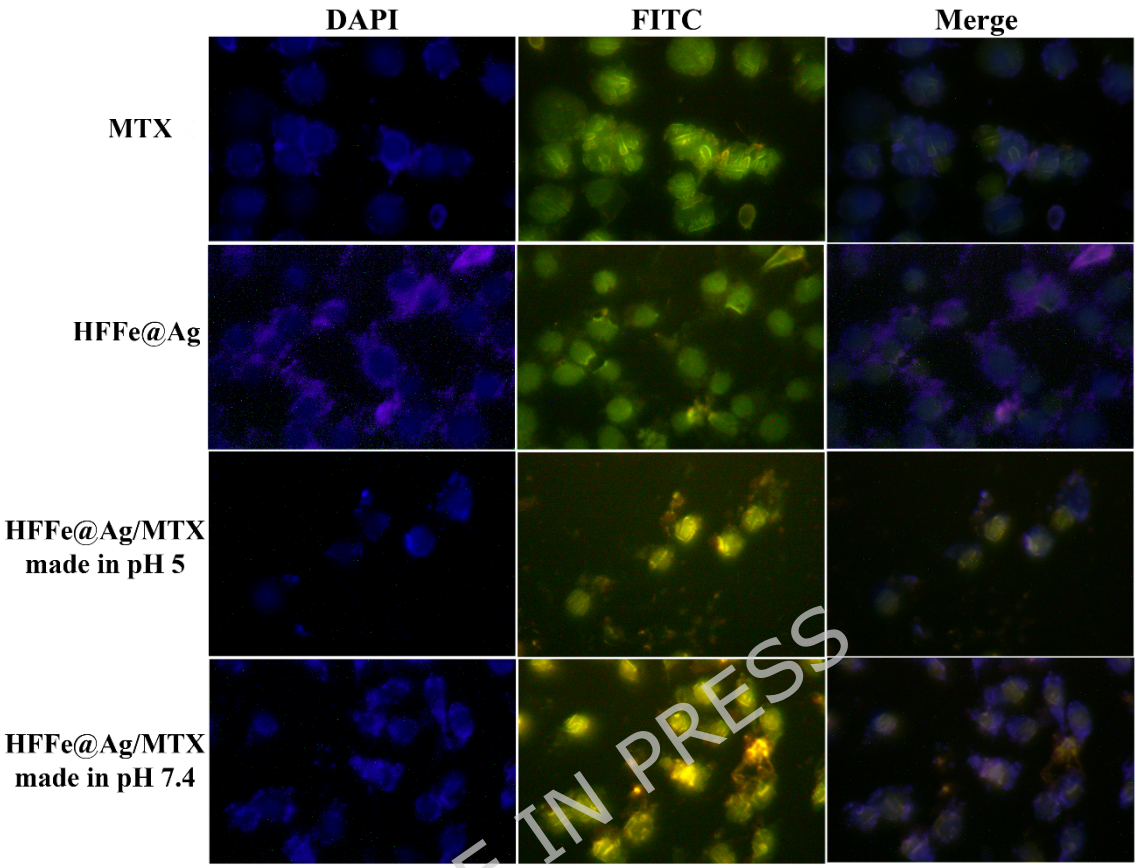

Figure 16. FITC labeled nanostructure image of L-929 cell line.

3.4.4. Hemolysis assay HFAg-Fe/MTX

The hemocompatibility of the HFAg-Fe/MTX was investigated through hemolysis experiments. Diluted whole blood utilized for assessing hemolytic properties of nanoparticles according to ASTM E2524 standard.

The percentages of hemolysis in the samples were calculated by comparing their absorbance with the positive and negative controls, using the following equation:

$$Percentage\ hemolysis = \frac{\text{Absorbance of sample-Absorbance of negative control}}{\text{Absorbance of positive control- Absorbance of negative control}} \times 100$$

This method is based on colorimetric absorbance of red-colored cyanmethemoglobin in Drabkin's reagent at 540nm. The measured absorbance is compared to a standard curve to determine the concentration of hemoglobin in the supernatant, and this hemoglobin concentration is compared to blank to obtain the percentage particle-induced hemolysis.

The percentage of hemolysis for all samples, except those with HFAg-Fe concentrations of 1.6 and 3.2 mg/mL, was below 5%, indicating that the test material is generally safe and biocompatible (Figure 17). The increased hemolysis observed at higher concentrations of HFAg-Fe may be attributed to the presence of free functional groups on the carrier surface. Additionally, variations in sample processing pH did not significantly affect the hemolysis rate, and the drug-loaded nanoparticle samples exhibited no hemolytic activity.

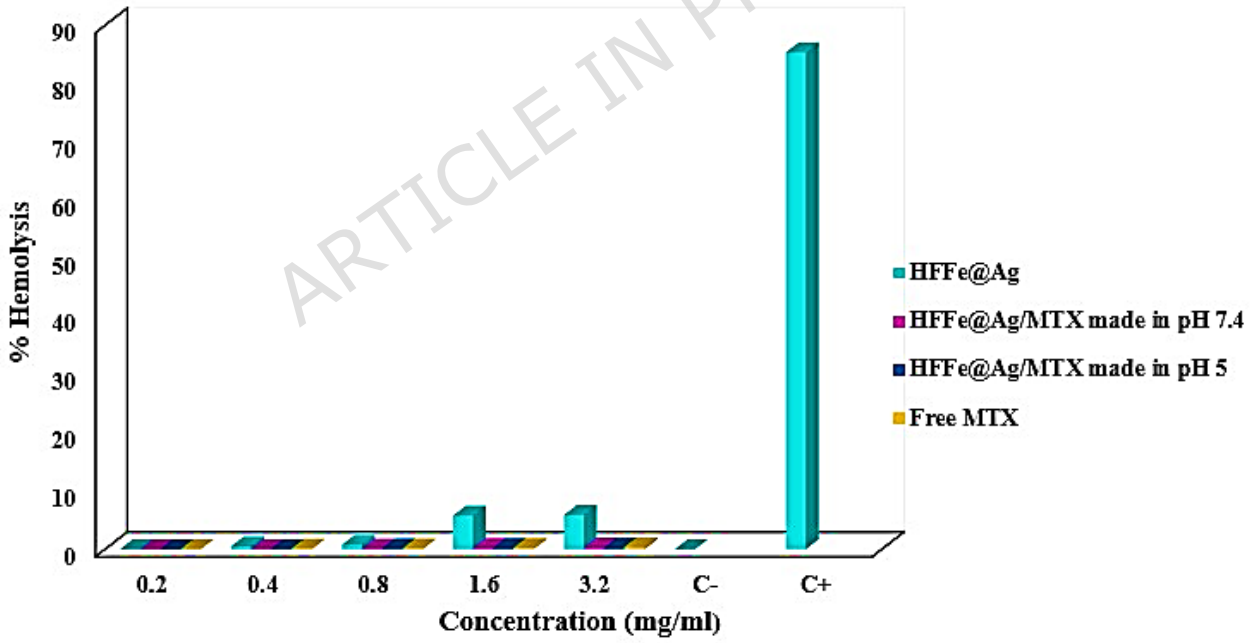

Figure 17. Hemolysis (%) of the HFAg-Fe, HFAg-Fe/MTX (pH= 7), HFAg-Fe/MTX (pH= 6) and free MTX.

3.4.5. Micro-CT Scan images

The region of interest (ROI) was extracted for sample using a circular mask, and the Linear attenuation coefficient (μ) of each material was calculated. The contrast and Hounsfield unit values were calculated based on the linear attenuation coefficient as described previously.

The results and the 2D Micro-CT image are shown in Table 3 and Figure 18, respectively.

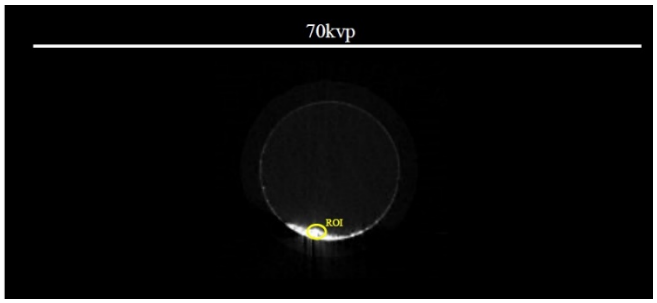

Figure 18. 2D micro-CT images of the sample (HFAg-Fe). The region of interest is indicated by a yellow circle.

Table 3. Linear attenuation coefficient, contrast criteria, and Hounsfield unit for each sample at 70 kVp.

Sample	Linear attenuation coefficient (μ, cm^{-1})	Contrast	Hounsfield Unit (HU)
HFAg-Fe	0.493	0.867	13097.3
Water	0.0350	0	0

We conducted a study to evaluate the therapeutic efficacy and biodistribution of the MTX administered in a breast cancer model using CT imaging. The treatment duration was 14 days, during which the drug was administered *via* intravenous injection every two days. Imaging sessions were performed at baseline (Blank, A), on a day 1(B), 7(C), and 14 (D) to assess tumor response and drug distribution. Baseline CT imaging established the initial tumor size

and morphological changes, indicating a positive response to treatment over the 14-day period. Analysis of the imaging data revealed that (white arrow), CT imaging revealed a significant accumulation of HFAg-Fenanostructures within the tumor region, resulting in enhanced contrast. This observation is attributed to the plasmonic and X-ray attenuation properties of the Ag-based nanoflowers rather than the methotrexate itself, which is radiolucent. with minimal distribution to adjacent normal tissues and other organs. This selective accumulation was consistently observed across multiple imaging time points and is attributed to passive tumor targeting via the enhanced permeability and retention (EPR) effect. across multiple imaging time points, confirming the drug’s preferential localization to the tumor site as illustrated in the representative CT images. Overall, the findings from our CT imaging suggest that the administered drug effectively targets the tumor, leading to a significant

tumor size reduction without appreciable distribution to other organs (Figure 19).

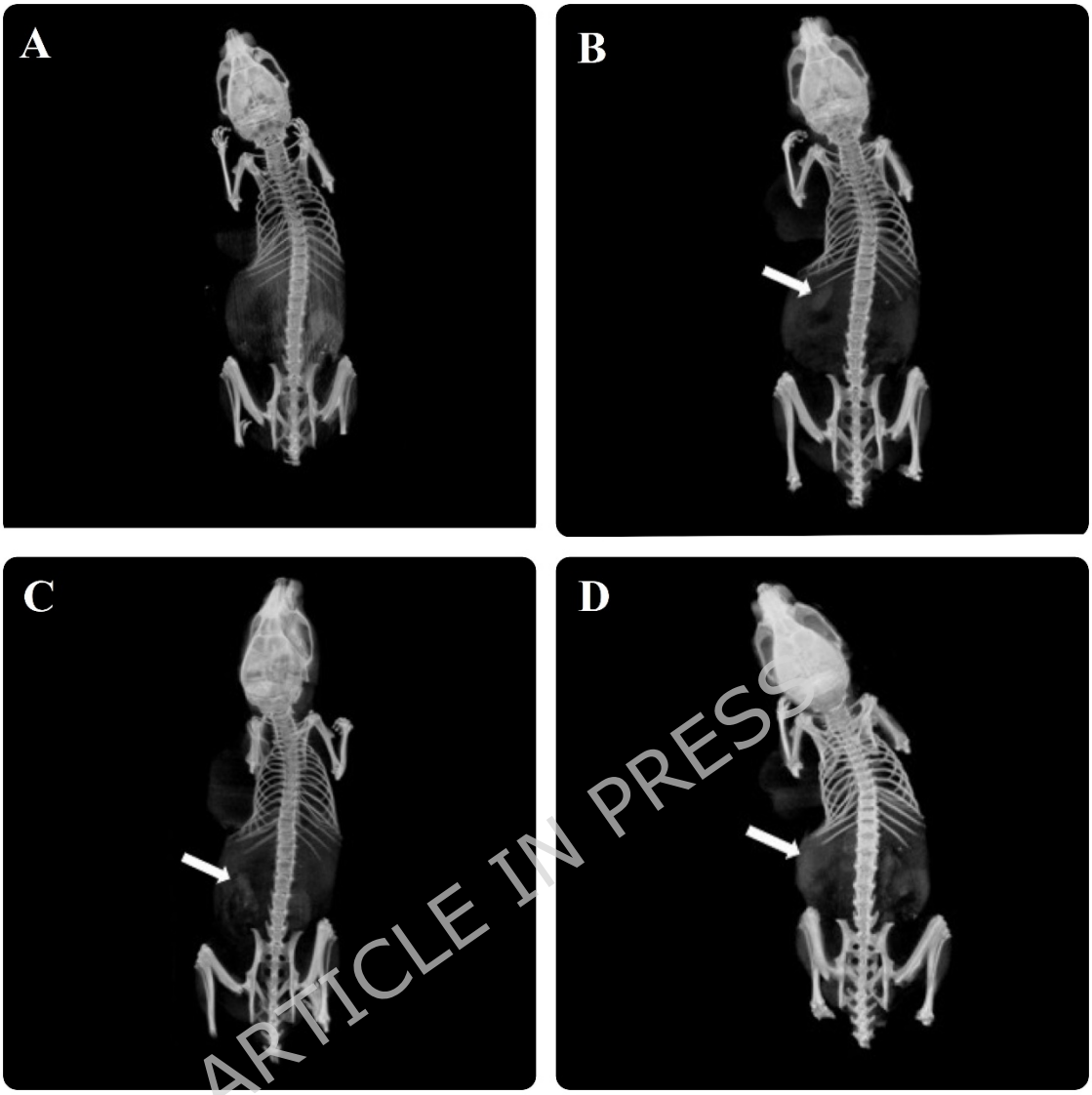

Figure 19. CT images of a breast cancer model in mice at baseline (A), and following treatment on days 1 (B), 7(C), and 14(D)

3.4.6. Histopathological analysis of tissue

Histological study of the liver (A-D) and spleen (E-H) tissues from breast cancer model mice, subjected to H&E staining on days 1, 7, and 14 post-treatments, provided deeper and clearer insights into the pharmacokinetics of the administered drug (Figure 20). Our findings revealed that, on days 7 and 14

post-administration, the drug accumulation in the liver and spleen was minimized. On day 7, drug presence significantly decreased, indicating a transient circulation phase, while by day 14, there was a marked increase in drug deposits in both hepatic and splenic tissues (C&D-G&H). These results highlight the dynamic behavior of the drug in the bloodstream and its pharmacological responses within various organs.

Most importantly, the analysis revealed that the drug did not show significant distribution in other organs throughout the study period. This selective accumulation pattern in the liver and spleen clearly indicates surface-functionalized drug delivery system drug uptake by the tumor microenvironment. This suggests that the drug's specific targeting is due to complex interactions with the tumor's vascular structure, particularly in regions with high blood flow and compromised vascular integrity.

Given the unique characteristics of flower-like nanostructures, these nanostructures, despite their micrometer size, are able to effectively penetrate the tumor region. This tumor penetration capability is primarily attributed to the "Enhanced Permeability and Retention" (EPR) effect, which is observed in areas with high blood flow and disrupted vascular structures in tumors. Specifically, even micrometer-sized nanostructures can selectively accumulate in the tumor microenvironment [53].

These findings decisively demonstrate that the drug predominantly accumulates in the tumor microenvironment, providing new evidence to advance breast cancer treatment through targeted drug delivery to specific tumor regions. Thus, the results of this study underscore the significance of

utilizing these nanostructures in cancer therapy and pave the way for future research and developments aimed at enhancing therapeutic efficacy.

Furthermore, these nanostructures, with their ability to encapsulate the drug and target the tumor directly, can resolve issues related to the toxicity and improper distribution of methotrexate. By leveraging the EPR effect, these nanostructures can selectively deliver the drug to the tumor’s damaged regions, preventing drug accumulation in off-target organs and ensuring more efficient and safer therapeutic outcomes.

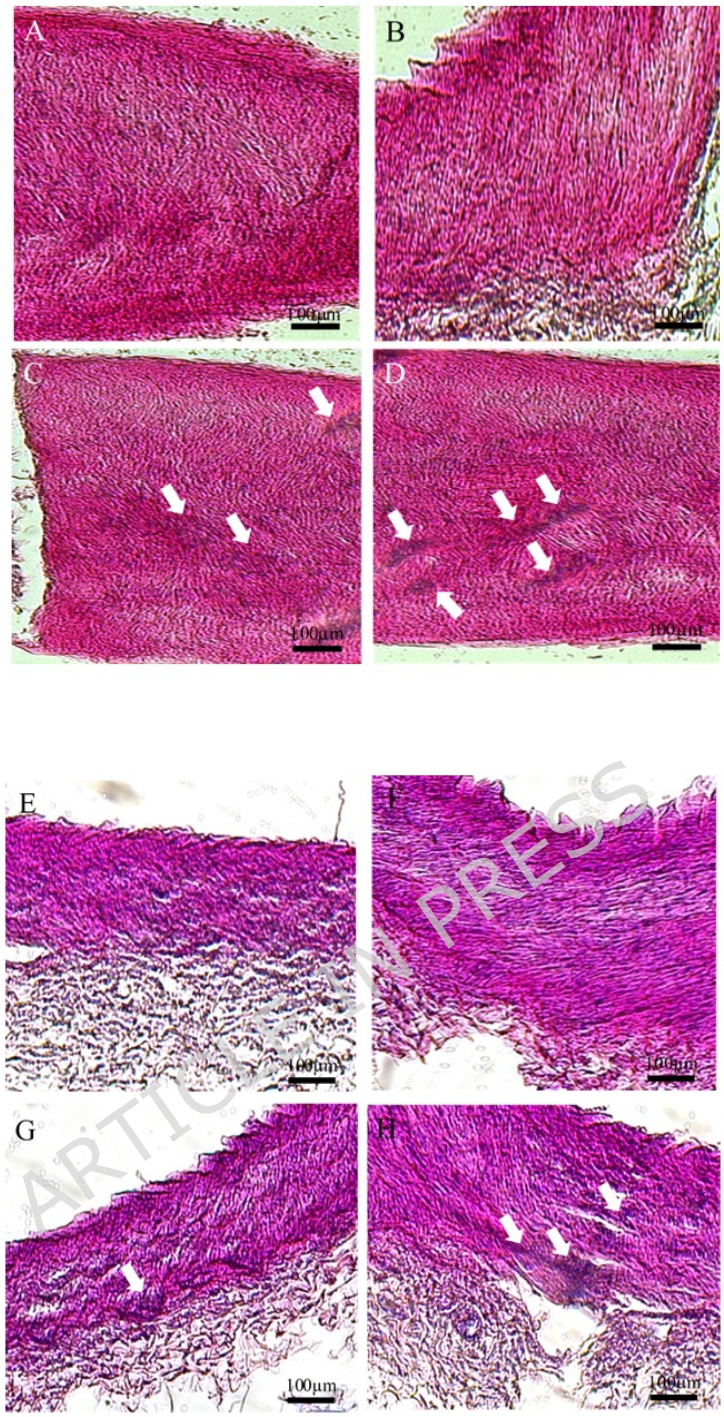

Figure 20. H & E staining of liver tissues including Normal group (A), Day 1(B), Day 7(C), Day 14(D), also, Normal group (E), Day 1(F), Day 7(G), Day 14(H) in spleen tissue. White arrows show accumulation of drugs after days 7 and 14. (magnification, 100×)

3.4.7. Histopathological analysis of tumor tissue

Histopathological evaluation of tumor tissues revealed clear time-dependent therapeutic effects following treatment with HFAg-Fe/MTX (Figure 21).

Tumors from the control group displayed intact nuclei and minimal necrotic features, indicative of aggressive tumor progression. In treated groups, early pathological alterations were observed on day 1, including mild cellular disruption and initial nuclear condensation. By day 7, significant tumor degeneration became apparent, characterized by reduced cellular density, disorganized tumor architecture, and the emergence of necrotic regions. These effects were further intensified by day 14, with extensive areas of coagulative necrosis and pronounced tissue destruction. In addition to tumor necrosis, localized dense deposits were observed within the tumor sections of treated groups, particularly on days 7 and 14 (indicated by arrows in Figure 21). These regions are attributed to the accumulation of drug-loaded HFAg-Fe nanostructures within the tumor microenvironment. The presence of these deposits is consistent with the biodistribution and CT imaging results, which demonstrated enhanced contrast arising from the Ag-based nanostructures rather than the drug itself.

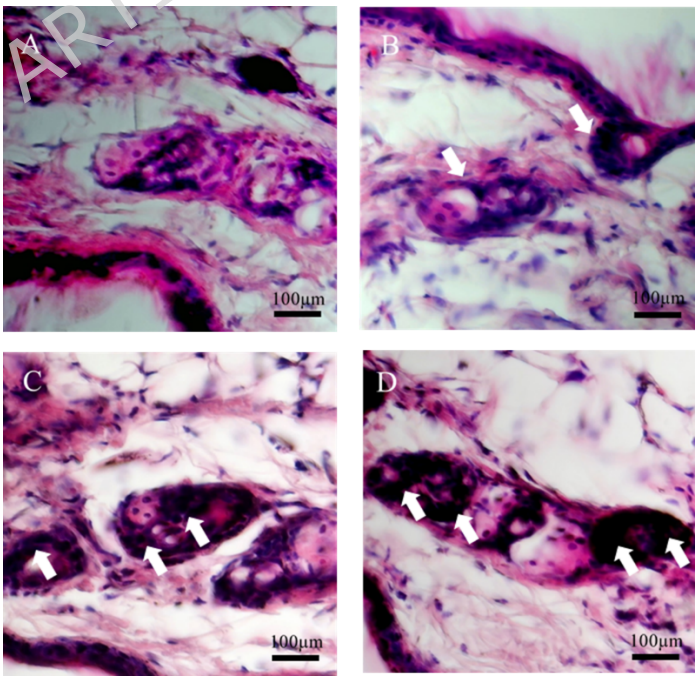

Figure 21. Histopathological analysis of tumor tissues from breast cancer bearing mice following treatment with HFAg-Fe/MTX. Representative

hematoxylin and eosin (H&E) stained tumor sections from (A) control group, (B) day 1, (C) day 7, and (D) day 14 post-treatment. Progressive tumor damage, including extensive necrotic regions, is evident over time. The arrows indicate regions of localized accumulation of drug-loaded nanostructures within the tumor tissue, appearing as dense deposits particularly pronounced on days 7 and 14. (magnification of 100×).

4. Conclusion

In summary, this study demonstrates the successful synthesis and comprehensive characterization of three-dimensional hierarchical flower-like iron-doped silver nanostructures (HFAg-Fe) as an innovative and highly efficient platform for surface-functionalized drug delivery system drug delivery. The HFAg-Fe nanocarriers exhibited remarkable methotrexate (MTX) loading capacity and a desirable pH-responsive release profile, ensuring accelerated drug release under acidic tumor microenvironment conditions while minimizing off-target effects at physiological pH. Hemocompatibility and cytotoxicity assessments confirmed the excellent biocompatibility of HFAg-Fe/MTX, with enhanced anticancer efficacy compared to free MTX, particularly against breast cancer cells. Imaging and biodistribution studies further supported the selective accumulation and therapeutic potential of the nanocarrier system within tumor tissues.

These findings highlight the promise of HFAg-Fe nanostructures as a versatile and safe drug delivery platform, capable of addressing key challenges in cancer therapy such as surface-functionalized drug delivery system delivery, controlled release, and reduced cytotoxicity. The modular design of these nanostructures also opens avenues for the incorporation of other therapeutic agents or targeting ligands, broadening their applicability to a range of

diseases beyond cancer. Future studies should focus on detailed in vivo pharmacokinetics, long-term safety, and the potential for clinical translation of this platform. Overall, the HFAg-Fe system represents a significant advancement in the development of next-generation nanomedicine for effective and precise cancer treatment.

Notes

All procedures involving live vertebrate animals were reviewed and approved by the Tehran Preclinical Core Facility (TPCF) based at Tehran University of Medical Sciences Animal Care lab (certificate No.: QMS0334040617) and fully complied with ISO 10993-2 requirements for animal welfare. Efforts were made to minimize animal suffering and reduce the number of animals used. Animal care, housing, and accommodation met or exceeded national and international guidelines referenced in ISO 10993.

Data Availability Statement

All data generated or analyzed during this study are included in this published article.

Funding Acknowledgements

We are grateful to the Iranian National Science Foundation (INSF) project number 4028201 for financial support for the research of this work.

Author Contributions

W.M. Methodology, Validation, Investigation, Writing Original Draft. **A.L.I.** Conceptualization, Writing Review and Editing, Methodology, Data Curation. **M.M.** Conceptualization, Resources, Writing, Review and Editing, Supervision,

Project administration, Funding acquisition. **M.R.** Methodology, Writing Original Draft. **V.A.** Writing Review and Editing, Visualization. **F.K.** Methodology, Investigation. **S.T, I.M.B, V.M** Conceptualization and Supervision.

Declaration of interests

The authors declare that they have no known competing financial interests or personal relationships that could have appeared to influence the work reported in this paper.

References:

1 Zeb, A., Gul, M., Nguyen, T.-T.-L. & Maeng, H.-J. Controlled release and targeted drug delivery with poly (lactic-co-glycolic acid) nanoparticles: reviewing two decades of research. *Journal of Pharmaceutical Investigation* **52**, 683-724 (2022).

2 Karami, M. H., Abdouss, M. & Maleki, B. The state of the art metal nanoparticles in drug delivery systems: A comprehensive review. *Nanomedicine Journal* **11** (2024).

3 Li, W. *et al.* Hierarchical drug release designed Au@ PDA-PEG-MTX NPs for targeted delivery to breast cancer with combined photothermal-chemotherapy. *Journal of Nanobiotechnology* **19**, 1-15 (2021).

4 Mukhtar, M. *et al.* Nanocarriers for methotrexate delivery/codelivery in the frame of cancer diagnostics and treatment: a review. *Frontiers in Biomaterials Science* **2**, 1200670 (2023).

5 Taran, Z. *et al.* Methotrexate loaded in alginate beads for controlled drug release against breast cancer. *Gene* **851**, 146941 (2023).

6 Zarbab, A., Sajjad, A., Rasul, A., Jabeen, F. & Iqbal, M. J. Synthesis and characterization of Guar gum based biopolymeric hydrogels as carrier materials for controlled delivery of methotrexate to treat colon cancer. *Saudi Journal of Biological Sciences* **30**, 103731 (2023).

7 Liu, R. *et al.* Advances of nanoparticles as drug delivery systems for disease diagnosis and treatment. *Chinese chemical letters* **34**, 107518 (2023).

8 Khodashenas, B., Ardjmand, M., Rad, A. & Esfahani, M. Gelatin-coated gold nanoparticles as an effective pH-sensitive methotrexate drug delivery system for breast cancer treatment. *Materials Today Chemistry* **20**, 100474 (2021).

9 Ramezanian, S., Moghaddas, J., Roghani-Mamaqani, H. & Rezamand, A. Dual pH-and temperature-responsive poly (dimethylaminoethyl methacrylate)-coated mesoporous silica nanoparticles as a smart drug delivery system. *Scientific Reports* **13**, 20194 (2023).

10 Cheralayikkal, S., Manoj, K. & Hussan, K. S. Formulation and evaluation of a smart drug delivery system of 5-fluorouracil for pH-sensitive chemotherapy. *Heliyon* **8** (2022).

11 Lestari, W., Wahyuningsih, S., Gomez-Ruiz, S. & Wibowo, F. in *Journal of Physics: Conference Series.* 012032 (IOP Publishing).

12 Mansour, A., Fytory, M., Ahmed, O. M., Rahman, F. E.-Z. S. A. & El-Sherbiny, I. M. In-vitro and in-vivo assessment of pH-responsive core–shell nanocarrier system for sequential delivery of methotrexate and 5-fluorouracil for the treatment of breast cancer. *International Journal of Pharmaceutics* **648**, 123608 (2023).

13 Chandrakala, V., Aruna, V. & Angajala, G. Review on metal nanoparticles as nanocarriers: Current challenges and perspectives in drug delivery systems. *Emergent Materials* **5**, 1593-1615 (2022).

14 Widiyanti, P., Theja, M. L. & Zaidan, A. H. in *AIP Conference Proceedings.* (AIP Publishing).

15 Shi, L. *et al.* Hierarchical magnetic nanoparticles for highly effective capture of small extracellular vesicles. *Journal of Colloid and Interface Science* **615**, 408-416 (2022).

16 Yuan, E. *et al.* Constructing hierarchical structures of Pd catalysts to realize reaction pathway regulation of furfural hydroconversion. *Journal of Catalysis* **421**, 30-44 (2023).

17 Zhou, C., Wang, M. & Yang, F. Gas sensing properties of WO3 based materials with hierarchical structural features. *Ceramics International* (2024).

18 Wawrzyńczak, A., Nowak, I., Woźniak, N., Chudzińska, J. & Feliczak-Guzik, A. Synthesis and Characterization of Hierarchical Zeolites Modified with Polysaccharides and Its Potential Role as a Platform for Drug Delivery. *Pharmaceutics* **15**, 535 (2023).

19 Wang, B. *et al.* A micro/nano-multiscale hierarchical structure strategy to fabricate highly conducting films for electromagnetic interference shielding and energy storage. *Journal of Materials Chemistry A* **11**, 8656-8669 (2023).

20 Ghitman, J. & Voicu, S. I. Controlled drug delivery mediated by cyclodextrin-based supramolecular self-assembled carriers: From design to clinical performances. *Carbohydrate Polymer Technologies and Applications* **5**, 100266 (2023).

21 Strukov, G., Strukova, G., Leonard, M. & Kuklja, M. M. Biomimetic In Situ Self-Assembly of Metal Nanoparticles into Hierarchical 3D Mesostructures: Synthesis, Analysis, and Prospects. *Crystal Growth & Design* (2024).

22 Liu, T., Li, D., Yang, D. & Jiang, M. Fabrication of flower-like silver structures through anisotropic growth. *Langmuir* **27**, 6211-6217 (2011).

23 Sarode, A., Annapragada, A., Guo, J. & Mitragotri, S. Layered self-assemblies for controlled drug delivery: A translational overview. *Biomaterials* **242**, 119929 (2020).

24 Huang, Q. & Zhu, X. Synthesis of 3D hierarchical Ag microspheres assembled with dendritic morphology. *Materials Chemistry and Physics* **138**, 689-694 (2013).

25 Deshmukh, A. R. & Kim, B. S. Flower-like biogenic gold nanostructures for improved catalytic reduction of 4-nitrophenol. *Journal of Environmental Chemical Engineering* **9**, 106707 (2021).

26 He, J. *et al.* Biomineralized synthesis of palladium nanoflowers for photothermal treatment of cancer and wound healing. *International Journal of Pharmaceutics* **615**, 121489 (2022).

27 Abed, A. *et al.* Platinum nanoparticles in biomedicine: Preparation, anti-cancer activity, and drug delivery vehicles. *Frontiers in Pharmacology* **13**, 797804 (2022).

28 Bhosale, S. V., Al Kobaisi, M., Jadhav, R. W. & Jones, L. A. Flower-Like Superstructures: Structural Features, Applications and Future Perspectives. *The Chemical Record* **21**, 257-283 (2021).

29 Suber, L. & Campi, G. Hierarchic self-assembling of silver nanoparticles in solution. *Nanotechnology Reviews* **1**, 57-78 (2012).

30 El-Nagar, G. A. *et al.* Efficient 3D-silver flower-like microstructures for non-enzymatic hydrogen peroxide (H2O2) amperometric detection. *Scientific Reports* **7**, 12181 (2017).

31 Gu, Y. *et al.* Defect engineered nickel hydroxide nanosheets for advanced pseudocapacitor electrodes. *Nano Research*, 1-10 (2024).

32 Sarhan, R. M., El-Nagar, G. A., Abouserie, A. & Roth, C. Silver–iron hierarchical microflowers for highly efficient H2O2 nonenzymatic amperometric detection. *ACS sustainable chemistry & engineering* **7**, 4335-4342 (2019).

33 Rezaei, S. *et al.* Development of a novel bi-enzymatic silver dendritic hierarchical nanostructure cascade catalytic system for efficient conversion of starch into gluconic acid. *Chemical Engineering Journal* **356**, 423-435 (2019).

34 Nori, Z. Z. *et al.* Synthesis and characterization of a new gold-coated magnetic nanoparticle decorated with a thiol-containing dendrimer for targeted drug delivery, hyperthermia treatment and enhancement of MRI contrast agent. *Journal of Drug Delivery Science and Technology* **81**, 104216 (2023).

35 Kumar, M. P. *et al.* In vitro cytotoxicity evaluation of endodontic irrigants combined with cationic peptide. *Journal of Conservative Dentistry and Endodontics* **28**, 84-89 (2025).

36 Zohoorian-Abootorabi, T. *et al.* Modulation of cytotoxic amyloid fibrillation and mitochondrial damage of α-synuclein by catechols mediated conformational changes. *Scientific Reports* **13**, 5275 (2023).

37 Zolfagharian, S., Zahedi, P., Ardestani, M. S., Khatibi, A. & Jafarkhani, S. Sodium alginate/xanthan-based nanocomposite hydrogels containing 5-fluorouracil: Characterization and cancer cell death studies in presence of halloysite nanotube. *Journal of Industrial and Engineering Chemistry* **120**, 374-386 (2023).

38 Dobrovolskaia, M. A. *et al.* Method for analysis of nanoparticle hemolytic properties in vitro. *Nano letters* **8**, 2180-2187 (2008).

39 Sciences, C. f. I. O. o. M. *International ethical guidelines for health-related research involving humans: Prepared by the Council for International Organizations of Medical Sciences (CIOMS) in collaboration with the World Health Organization (WHO)*. (Council for International Organizations of Medical Sciences, 2016).

40 Bancroft, J. D. & Gamble, M. *Theory and practice of histological techniques*. (Elsevier health sciences, 2008).

41 El-Nagar, G. A., Lauermann, I., Sarhan, R. M. & Roth, C. Hierarchically structured iron-doped silver (Ag–Fe) lotus flowers for an efficient oxygen reduction reaction. *Nanoscale* **10**, 7304-7310 (2018).

42 Ta, Q. T. H., Cho, E., Sreedhar, A. & Noh, J.-S. Mixed-dimensional, three-level hierarchical nanostructures of silver and zinc oxide for fast photocatalytic degradation of multiple dyes. *Journal of Catalysis* **371**, 1-9 (2019).

43 Heli, H. & Yadegari, H. Nanoflakes of the cobaltous oxide, CoO: Synthesis and characterization. *Electrochimica Acta* **55**, 2139-2148 (2010).

44 Singh, D., Tiwari, A., Singh, R. P. & Singh, A. K. Clove bud extract mediated green synthesis of bimetallic Ag–Fe nanoparticles: antimicrobial, antioxidant and dye adsorption behavior and mechanistic insights of metal ion reduction. *Materials Chemistry and Physics* **311**, 128529 (2024).

45 Noor, A., Pant, K. K., Malik, A., Moyle, P. M. & Ziora, Z. M. Green Encapsulation of Metal Oxide and Noble Metal ZnO@ Ag for Efficient Antibacterial and Catalytic Performance. *Industrial & Engineering Chemistry Research* **64**, 10360-10372 (2025).

46 Gharebaghi, F., Dalali, N., Ahmadi, E. & Danafar, H. Preparation of wormlike polymeric nanoparticles coated with silica for delivery of methotrexate and evaluation of anticancer activity against MCF7 cells. *Journal of biomaterials applications* **31**, 1305-1316 (2017).

47 Fattahi, N., Bahari, A., Ramazani, A. & Koolivand, D. In vitro immunobiological assays of methotrexate-stearic acid conjugate in human PBMCs. *Immunobiology* **225**, 151984 (2020).
48 Cooper, I., Fridkin, M. & Shechter, Y. Conjugation of Methotrexate-Amino Derivatives to Macromolecules through Carboxylate Moieties Is Superior Over Conventional Linkage to Amino Residues: Chemical, Cell-Free and In Vitro Characterizations. *Plos one* **11**, e0158352 (2016).
49 Chee, C. F., Leo, B. F. & Lai, C. W. in *Applications of nanocomposite materials in drug delivery* 861-903 (Elsevier, 2018).
50 Li, G. & Szostak, M. Transition-metal-free activation of amides by N− C bond cleavage. *The Chemical Record* **20**, 649-659 (2020).
51 Wu, Z., Liu, C., Zhang, Z., Zheng, R. & Zheng, Y. Amidase as a versatile tool in amide-bond cleavage: From molecular features to biotechnological applications. *Biotechnology Advances* **43**, 107574 (2020).
52 Nogueira, D. R. *et al.* In vitro antitumor activity of methotrexate via pH-sensitive chitosan nanoparticles. *Biomaterials* **34**, 2758-2772 (2013).
53 Kang, H. *et al.* Size-dependent EPR effect of polymeric nanoparticles on tumor targeting. *Advanced healthcare materials* **9**, 1901223 (2020).